Article

Immunity

# Local antibody feedback enforces a checkpoint on affinity maturation in the germinal center and promotes epitope spreading

## Graphical abstract

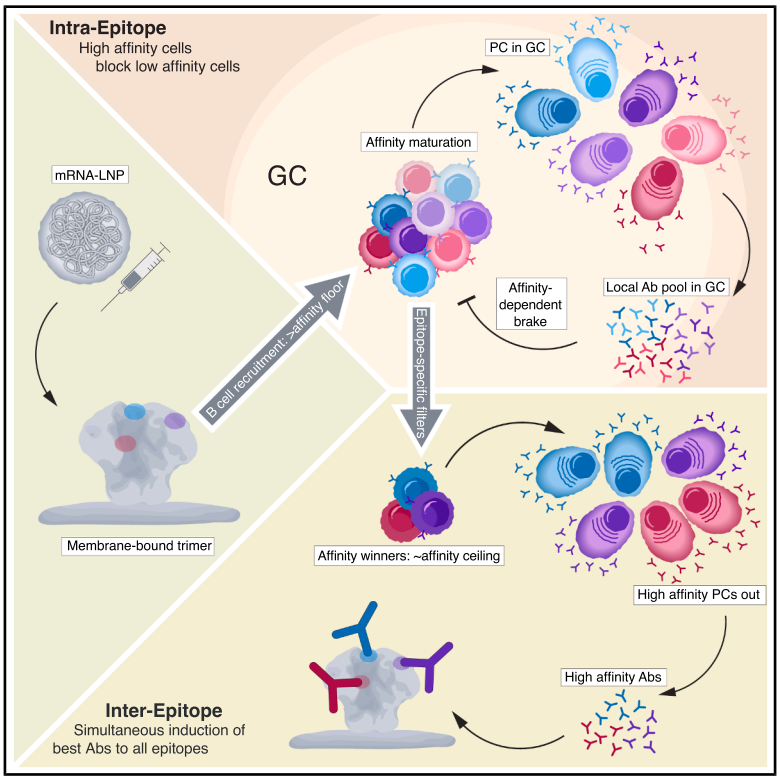


## Highlights

- One mRNA immunogen activated B cells to three different epitopes
- Higher-affinity B cells displayed shorter GC half-lives
- Local antibody feedback established intra-epitope GC affinity floors and ceilings
- Antibodies from local plasma cells determined GC kinetics

## Authors

Yu Yan (颜雨), Xuesong Wang (王雪松), Zhenfei Xie (谢振飞), ..., Sophia Liu, William R. Schief, Facundo D. Batista

## Correspondence

sophia.liu@mgh.harvard.edu (S.L.), schief@scripps.edu (W.R.S.), fbatista1@mgh.harvard.edu (F.D.B.)

## In brief

Feedback from circulating antibodies can shape initiating immune responses. Yan et al. examine ongoing germinal center (GC) responses upon immunization with an mRNA-LNP-encoded membrane-bound immunogen displaying three conserved HIV-1 envelope epitopes and find antibody-mediated intra-epitope competitive effects and a contribution of local antibodies to determining B cell residency in GCs and affinity maturation.

Yan et al., 2026, Immunity *59*, 746–767
March 10, 2026 
https://doi.org/10.1016/j.immuni.2026.01.011

CellPress

CellPress
OPEN ACCESS

Immunity

Article

# Local antibody feedback enforces a checkpoint on affinity maturation in the germinal center and promotes epitope spreading

Yu Yan (颜雨),[1,12] Xuesong Wang (王雪松),[1,12] Zhenfei Xie (谢振飞),[1,12] Daniel L.V. Bader,[2,3,4,7,13] Ryan H. Lim,[5,6,13] Krystal M. Ma,[2,4,7] Christopher A. Cottrell,[2,4,7] Jon M. Steichen,[2,4,7] Liling Xu (徐利玲),[1] Paula M. Villavicencio,[1] Madhav Akauliya,[1] Ja-Hyun Koo,[1] Jacqueline Ming Shen,[1,9] Alexandra Vernich,[5] Oleksandr Kalyuzhniy,[2,4,7] Joel D. Allen,[4,8] Ali A. Albowaidey,[1] Anthony Alicea,[1] Bingxian Chen,[1,5] Erik Georgeson,[2,4,7] Jordan Renae Ellis-Pugh,[1] Nushin Alavi,[2,4,7] Abigail Esposito,[1] Hannah Naili,[1] Nicole Phelps,[2,4,7] Brendon Kelley,[1] Michael Kubitz,[2,4,7] Quynh Anh Phan,[1] Alessia Liguori,[2,4,7] Thavaleak Prum,[1] Ryan Tingle,[2,4,7] Danny Lu,[2,4,7] Saman Eskandarzadeh,[2,4,7] Xiaotie Liu,[1] John E. Warner,[1] Stephanie R. Weldon,[1] Sunny Himansu,[10] Max Crispin,[4,8] Usha Nair,[1] Sophia Liu,[5,*] William R. Schief,[2,4,7,10,*] and Facundo D. Batista[1,9,11,14,*]

[1]Batista Laboratory, Ragon Institute of Mass General Brigham, MIT, and Harvard, Cambridge, MA 02139, USA
[2]Department of Immunology and Microbiology, The Scripps Research Institute, La Jolla, CA 92037, USA
[3]Department of Integrative Structural and Computational Biology, The Scripps Research Institute, La Jolla, CA 92037, USA
[4]Consortium for HIV/AIDS Vaccine Development (CHAVD), The Scripps Research Institute, La Jolla, CA 92037, USA
[5]Liu Laboratory, Ragon Institute of Mass General Brigham, MIT, and Harvard, Cambridge, MA 02139, USA
[6]Harvard-MIT Division of Health Sciences and Technology, Massachusetts Institute of Technology, Cambridge, MA 02139, USA
[7]IAVI Neutralizing Antibody Center, The Scripps Research Institute, La Jolla, CA 92037, USA
[8]School of Biological Sciences, University of Southampton, Southampton SO17 1BJ, UK
[9]Department of Biology, Massachusetts Institute of Technology, Cambridge, MA 02139, USA
[10]Moderna, Cambridge, MA 02142, USA
[11]Department of Immunology, Harvard Medical School, Boston, MA 02115, USA
[12]These authors contributed equally
[13]These authors contributed equally
[14]Lead contact
*Correspondence: sophia.liu@mgh.harvard.edu (S.L.), schief@scripps.edu (W.R.S.), fbatista1@mgh.harvard.edu (F.D.B.)
https://doi.org/10.1016/j.immuni.2026.01.011

## SUMMARY

Circulating antibodies from previous immune encounters impact subsequent humoral responses. Here, we investigated how local epitope-specific competition shapes ongoing germinal center (GC) responses by delivering an mRNA-LNP-encoded membrane-bound immunogen displaying three conserved HIV-1 envelope (Env) epitopes to mouse models bearing B cell receptors (BCRs) of defined affinities. High-affinity B cells exhibited shorter GC residency than lower-affinity counterparts. B cells engaged GC reactions at equivalent rates in the presence or absence of clonal lineages binding the same epitope with similar affinities; however, higher-affinity clones suppressed lower-affinity counterparts targeting the same epitope. Spatial transcriptomics revealed plasma-like cells within and adjacent to the GC, and early immunoglobulin G (IgG) was detectable in draining lymph nodes. Our findings suggest that a self-modulating local antibody feedback loop limits epitope-specific recognition—dampening selection for higher-affinity B cells and facilitating epitope spreading by redirecting the response toward alternative epitopes.

## INTRODUCTION

Affinity maturation is the fundamental process underpinning the humoral response to infection or vaccination.[1,2] Exposure to antigen activates a polyclonal B cell response derived from those cells with B cell receptors (BCRs) meeting a minimum affinity threshold.[3] Those with very high initial affinities will differentiate into extrafollicular plasma cells (PCs),[4] while others will form the germinal center (GC). GCs generate and diversify B cells: therein, somatic hypermutation (SHM) introduces mutations into the variable region of BCRs, producing further variation in affinity for the antigen.[5]

This expanded diversity is shaped by the pressure of competition in GC selection. Expansion in the GC is predicated upon survival and proliferation signals from T follicular helper (Tfh) cells.[6,7] B cells engage Tfh by presenting internalized antigen complexed with major histocompatibility complex class II (MHC class II).[8,9] The efficiency of this presentation is affinity dependent.[3,10] Though low-affinity clones can enter and participate in GCs, they may be excluded or disfavored in the presence

of higher-affinity competitors.[11–13] Lower-affinity B cells surviving in the GC may be selected for differentiation into memory B cells (MBCs),[14,15] but whether fate differentiation into MBC and long-lived PCs (LLPCs) is determined by BCR affinity is disputed,[16] and there is substantial variation in the affinity of antibodies expressed by PCs emerging from the GC.[17] Ultimately, slower antigen-BCR dissociation reaches a point of diminishing returns in terms of receptor activation enhancement, suggesting that, even if high-affinity cells appear early in the response, maturation in the GC reaches a ceiling above which affinity improvements are no longer visible to selection.[3,18,19] The antibodies of varying affinities produced by terminally differentiated B cells arising throughout this response may also shape the interactions of B cells in GCs.

Feedback from existing antibodies influences the downstream humoral response,[20–23] but its influence on the diversity of B cells entering and exiting GCs over the course of the response remains underexplored. Pre-existing antibody allows immune complex formation,[24] and the BCR affinity activation floor lowers for soluble antigens complexed with antibody.[3] Conversely, circulating antibodies may be competitive, intensifying selective pressure in GCs by limiting antigen access[25] or blocking cognate B cell entry.[26] Prior work from our group suggests a circulating antibody (Ab) affinity tipping point, with lower-affinity Abs enhancing GC responses and higher-affinity Abs blocking.[27] Antibodies thus affect B cell responses in dose, affinity, and epitope-specific manners.[28] However, when high-affinity monoclonal antibodies (mAbs) are present prior to SARS-CoV-2 immunization, a preponderance of low-affinity clones is observed in post-vaccination GCs.[29] This booster response is also characterized by a shift to subdominant epitopes. Breadth, and not potency alone, is an important determinant of protection—in malaria, vaccine-boosting Abs from prior vaccination limit overall recall responses, but those later responses are characterized by a shift toward subdominant epitopes.[30]

Feedback may be particularly important for vaccines requiring a longer immune response, multiple boosts, or multiple epitopes. Those are characteristics of HIV-1 retrovaccinology based on broadly neutralizing antibodies (bnAbs) to conserved epitopes on the HIV envelope (Env). In "germline-targeting" (GT) strategies, priming immunogens are designed for high affinity to the unmutated B cells inferred to give rise to bnAbs. These precursors are often rare and lack affinity to the mature HIV trimer.[31–42] After priming, several boosts with sequentially more native-Env-like immunogens may be required to guide precursors toward functional anti-HIV bnAbs.[32,39,41,43] An effective vaccine may need to elicit bnAbs to two or more distinct epitopes on Env to prevent viral escape.[44–50] Individuals undergoing these proposed vaccination schedules would thus have a variety of B cell lineages at varying affinities for conserved epitopes on Env and fluctuating antibody titers, converging on the same native trimer. A complicating factor is the capacity to introduce membrane-anchored antigen presentations via mRNA-lipid nanoparticles (LNPs). Increasing avidity by presenting antigen on a surface may lower the threshold for initial activation[51] or otherwise unpredictably alter the competitive environment.

Here, we established a series of late-stage HIV preclinical mouse models carrying human BCRs of known affinities to one of three epitopes on the HIV-1 Env: the CD4 binding site (CD4bs), V2-apex, and V3-glycan. These BCRs are "intermediate"—falling between germline and mature bnAbs in affinity and sequence evolution. By vaccinating variable-affinity preclinical B cell models with an mRNA-LNP encoding a single, membrane-anchored native trimer immunogen presenting all three epitopes, we found that lower-affinity cells reacted robustly to the trimer in isolation but that competition from higher-affinity lineages to the same epitope was inhibitory. Conversely, lower-affinity B cell lineages to the same epitope, and lineages with different epitope specificities, did not affect each other's GC kinetics. High-affinity antibodies alone reproduced inhibition, suggesting an antibody feedback mechanism. We furthermore identified local PCs within GCs as the likely sources of blocking antibody. Our findings provide insights into the mechanisms governing B cells within GCs and also offer guiding principles for the rational design of vaccines to elicit potent and broad antibody responses.

## RESULTS

### High-affinity BCR clones are efficiently recruited to GCs but are not preferentially maintained over lower-affinity counterparts

To investigate how inherent affinity affects GC kinetics following immunization with HIV-1 Env glycoproteins, we developed mouse models with BCRs derived from the phylogenies of human bnAbs (Figures S1A–S1C). We selected clinically relevant bnAbs targeting three non-overlapping neutralizing epitopes on the highly glycosylated HIV-1 Env: N6-I3 (CD4bs),[52,53] PCT64-18D (V2-apex),[54] and minBG18.6 (V3-glycan) (Figures S1D–S1F).[40] Using our CRISPR-Cas9 homologous directed recombination method,[55,56] we generated transgenic mouse models with B cells expressing the heavy chains (HCs) and/or light chains (LCs) of these three Abs. Lines were bred to homozygosity before use. Follicular cell development was normal, and though lines showed some variation in peritoneal B cells, all expected populations were present (Figures S1G and S1H). B cells isolated from these lines survived, differentiated, and proliferated at normal rates *in vitro* (Figure S1I). Peripheral blood mononuclear cells (PBMCs) in the resulting $IgH^{N6\text{-}I3/N6\text{-}I3}Ig\kappa^{N6\text{-}I3/N6\text{-}I3}$ (referred to as CD4bs-Int$^1$ below), $IgH^{PCT64\text{-}18D/PCT64\text{-}18D}Ig\kappa^{PCT64\text{-}18D/PCT64\text{-}18D}$ (V2-Int$^1$), and $IgH^{minBG18.6/\ minBG18.6}Ig\kappa^{WT/WT}$ (V3-Int$^1$) mouse lines were examined by 10× single-cell RNA sequencing (scRNA-seq). N6-I3 HC and N6-I3 LC sequences were co-expressed by 93.1% of cells from CD4bs-Int$^1$ mice, and PCT64-18D HC and PCT64-18D LCs by 99.7% of cells from V2-Int$^1$ mice, confirming intended BCR assembly. For V3-Int$^1$, HCs paired with diverse native murine LCs, most frequently IGLV1, IGKV4-68, IGKV4-61, IGKV12-98, and IGKV4-91 (Figure 1A).

We required an immunogen capable of activating B cells targeting diverse epitopes across a broad affinity range to evaluate how inherent BCR affinity impacts GC kinetics. BG505 MD39.3 gp151 (BG505 hereafter), which has performed well in non-human primates and a human clinical trial,[57,58] met that criterion. PBMCs from all three lines showed competent specific binding to BG505 and lack of binding to corresponding epitope knockout (KO) probes (Figures 1B and 1C). All three BCR variants showed detectable but varied affinities to BG505: the dissociation constant [$K_D$s] of CD4bs-Int$^1$ was 3 nM, V2-Int$^1$ 770 nM, and V3-Int$^1$, where the

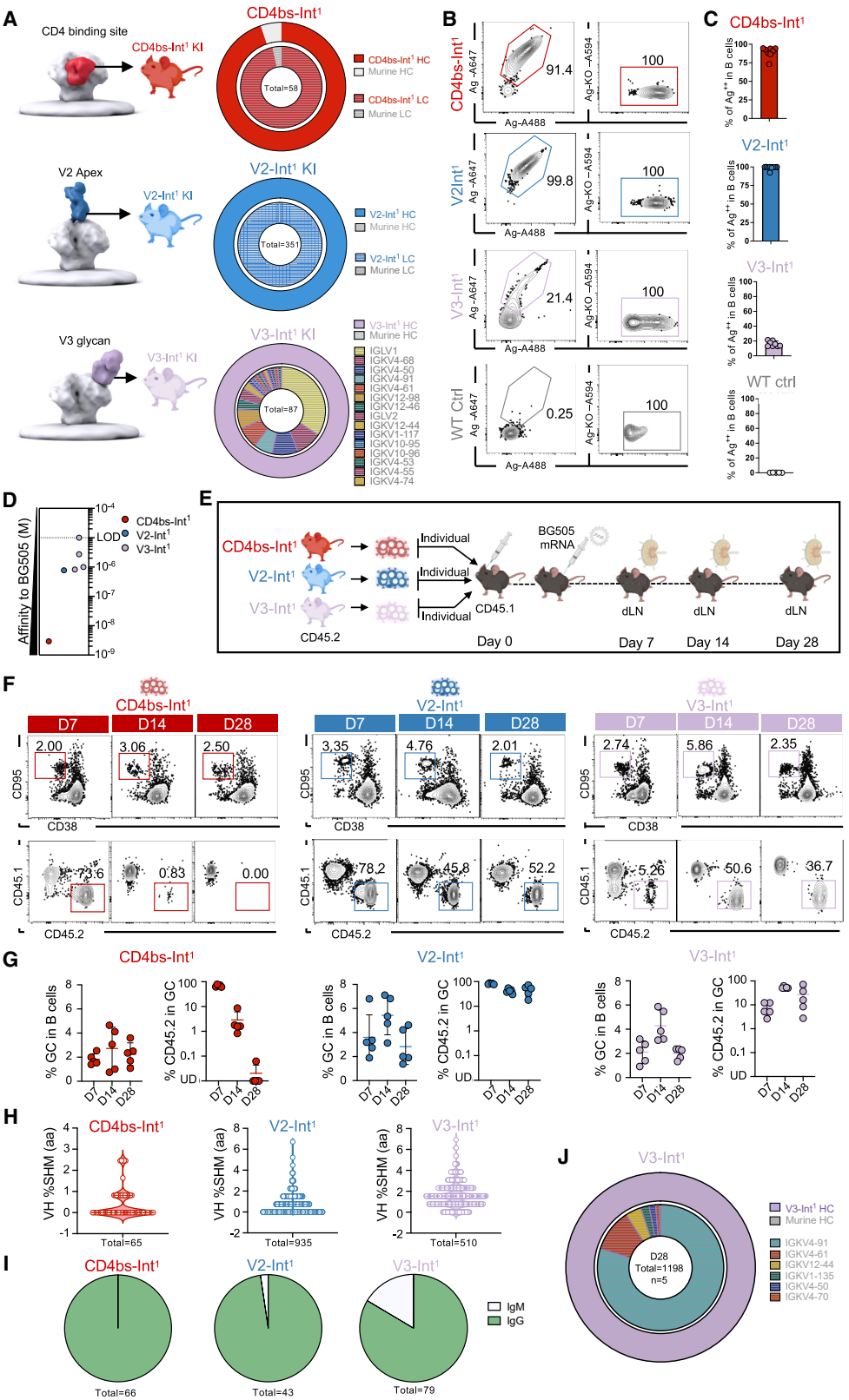


*(legend on next page)*

minBG18.6 HC paired with representative mouse LCs, ranged from 820 nM to the limit of detection (LOD) at 10 μM (Figure 1D).

CD4bs-Int$^1$, V2-Int$^1$, or V3-Int$^1$ CD45.2$^{+/+}$ cells were adoptively transferred into wild-type (WT) CD45.1$^{+/+}$ hosts individually to reach frequencies of 20 in $10^6$, and recipient mice were then immunized with an mRNA-LNP-encoded membrane-anchored BG505 (Figure 1E). The GC response and the proportion of CD45.2$^+$ B cells in GCs were evaluated in draining lymph nodes (dLNs) at days 7, 14, and 28. Across all transfer recipients, GCs constituted ~2%–5% of B cells on average (Figures 1F and 1G). CD45.2$^+$ cells from each line were effectively activated and present in GCs at D7, though their average fractions in GCs ranged from 5% for V3-Int$^1$ to 67% for CD4bs-Int$^1$ and 78% for V2-Int$^1$. At days 14 and 28, V2-Int$^1$ and V3-Int$^1$ CD45.2 B cells retained a share of the GC (43% and 47% for V2-Int$^1$, 53% and 27% for V3-Int$^1$). V3-Int$^1$ responses displayed higher variability at day 28, consistent with their polyclonality. CD4bs-Int$^1$ cells, which have the highest affinity for their epitope ($K_D$, 3 nM), dropped to 2.88% by day 14 and 0.16% at day 28 (Figures 1F and 1G). Sequencing by single-cell BCRseq of sorted antigen-specific CD45.2$^+$ B cells at day 21 revealed that immunization stimulated class switching and SHM in all three cell lines (Figures 1H, 1I, and S1J). Immunization selected for particular V3-Int$^1$ BCRs, with a shift toward IGKV4-91 (79.88%) and IGKV4-61 (10.93%) (Figures 1A and 1J). Thus, independent of initial affinity, all three cell lines could be stimulated by an mRNA-LNP-delivered membrane-anchored immunogen, enter the early GC, and undergo class switching and SHM, but each line displayed distinct GC kinetics, with a shorter GC half-life for the line with the highest initial affinity.

## High-affinity clones do not influence GC dynamics of low-affinity B cells targeting other epitopes

We next sought to determine whether the different B cell lines would compete despite targeting different epitopes on the same trimer. CD4bs-Int$^1$, V2-Int$^1$, and V3-Int$^1$ CD45.2$^{+/+}$ B cells were adoptively transferred into WT CD45.1$^{+/+}$ mice individually to reach a frequency of 20 cells per $10^6$ total B cells, or in equal-proportion combinations to reach 20 (1× mix) or 60 (3× mix) cells per $10^6$ total B cells. Total CD45.2$^{+/+}$ B cells in 1× mix matched individual transfer recipients. In the 3× mix, B cells from each individual CD45.2$^{+/+}$ line were at frequencies equivalent to individual transfers, but there were more total CD45.2$^{+/+}$ B cells. Recipient mice were immunized intramuscularly with 2 μg of BG505 mRNA-LNP 1 day later. Local, draining LNs were analyzed by flow cytometry at day 7 and day 21 post-immunization (Figure 2A). GC sizes were similar across groups at both time points. V2-Int$^1$ alone produced slightly larger GCs at day 7 than 3× mix, but this difference did not persist to day 21 (Figures 2B and 2C). Mice transferred with V3-Int$^1$ alone averaged fewer CD45.2$^+$ B cells in GCs at day 7 relative to recipients of other individual transfers or either mix, but no significant differences were observed at day 21 (Figure 2D). To determine the composition of the CD45.2 B cells in the mixed transfer recipients, all CD45.2 cells in the GCs were sorted for 10× scRNA-seq. CD4bs-Int$^1$, V2-Int$^1$, and V3-Int$^1$ cells were recovered from both the 1× and 3× mix recipients at variable frequencies (Figure 2E). The ratio for each CD4bs-Int$^1$, V2-Int$^1$, or V3-Int$^1$ cell identified by scRNA-seq was multiplexed back to the CD45.2 cell percentages obtained by flow cytometry for each individual mouse to estimate specific single CD4bs-Int$^1$, V2-Int$^1$, or V3-Int$^1$ B cell rates in dLN B cells. The percentage of CD4bs-Int$^1$, V2-Int$^1$, and V3-Int$^1$ B cells among total B cells at day 21 was indistinguishable between single transfers and either 1× or 3× mix (Figures 2F and S2A). Slightly higher mutation rates were observed in all three B cell lines isolated from 1× mix recipients compared with individual transfer recipients. In 3× mix recipients, SHM was only increased for V3-Int$^1$ HCs (Figure S2B). No differences were observed in class-switching profiles or the identities of the three most common LCs found with V3-Int$^1$,

**Figure 1. An mRNA-encoded membrane-anchored BG505 native trimer recruits intermediate bnAb-precursor B cells targeting different epitopes on Env**

(A) (Top) Nested pie chart of CD4bs-Int$^1$ heavy chain (HC) (red), murine HC (gray), human CD4bs-Int$^1$ light chain (LC) (shaded red), and murine LC (shaded gray) sequences amplified from single-cell sorted epitope-specific (BG505$^+$KO$^-$) naive B cells in CD4bs-Int$^1$ mice. (Middle) As top for V2-Int$^1$ HC (blue), murine HC (gray), human V2-Int$^1$ LC (shaded blue), and murine LC (shaded gray). (Bottom) As prior for human V3-Int$^1$ HC (purple), murine HC (gray), and murine LC sequences (multi-colored). Outer rings represent HCs, and inner rings represent LCs. Data are shown from one representative of two experiments ($n$ = 1–2 mice). "Total" denotes single cells amplified. For V3-Int$^1$, the top 15 of 20 LCs amplified are listed.

(B) Representative fluorescence-activated cell sorting (FACS) plots of BG505-double-positive and BG505-epitope-specific-KO-negative peripheral B cells in (descending): naive CD4bs-Int$^1$, V2-Int$^1$, V3-Int$^1$ mice, or WT controls. Events were pre-gated on lymphocytes/singlets/CD4$^-$CD8$^-$F4/80$^-$Gr1$^-$/B220$^+$ B cells.

(C) Quantification of (B). BG505-specific binders in blood peripheral B cells. $n$ = 8–10 for CD4bs-Int$^1$, V2-Int$^1$, or V3-Int$^1$ mice, $n$ = 5 for WT, pooled from 2–4 individual experiments. Bars are mean + SD.

(D) Affinity of CD4bs-Int$^1$ or V2-Int$^1$ or V3-Int$^1$ Ab against BG505 trimer measured by surface plasmon resonance (SPR) dissociation constant. For V3-Int$^1$, Abs were expressed with human HC and representative murine LCs (see key resources table). Each dot represents the mean of 4 technical replicates. Dotted line marks LOD.

(E) Schematic of GC recruitment evaluation experiments for CD4bs-Int$^1$, V2-Int$^1$, or V3-Int$^1$ CD45.2 B cells. Immunization output panels below display representative data from one of at least two experiments with 3–5 mice per condition.

(F) Representative FACS plots of B cells obtained from dLNs after immunization with mRNA-LNP encoding BG505 Env glycoprotein trimer. Days post-immunization at top. Events pre-gated on lymphocytes/singlets/live/CD4$^-$CD8$^-$F4/80$^-$Gr1$^-$/B220$^+$ B cells and represent GC in B cells, or CD45.2 cells in GC.

(G) Time course plots of GC cells as a percentage of total B cells (left) and CD45.2$^+$ cells as a percentage of GC B cells (right). Values of zero were plotted as UD (undetected) on the $\log_{10}$ scale. Each dot represents one mouse. Bars are mean ± SD.

(H) Dotted violin plots of HC amino acid mutations across all sites at day 21. Each dot represents an HC sequence from one B cell.

(I) Pie charts of class-switch profiles at day 21. Total = sequences amplified.

(J) Nested pie chart showing V3-Int$^1$ HC and LC usage from single-cell sorted epitope-specific (BG505$^+$KO$^-$) B cells at day 28; no murine HC (gray) detected. Outer layer, human V3-Int$^1$ IGHV; inner layer, murine IGKV. Nested pie chart shows average of all mice in a group (total = sequences amplified, $n$ = mice).

See also Figure S1.

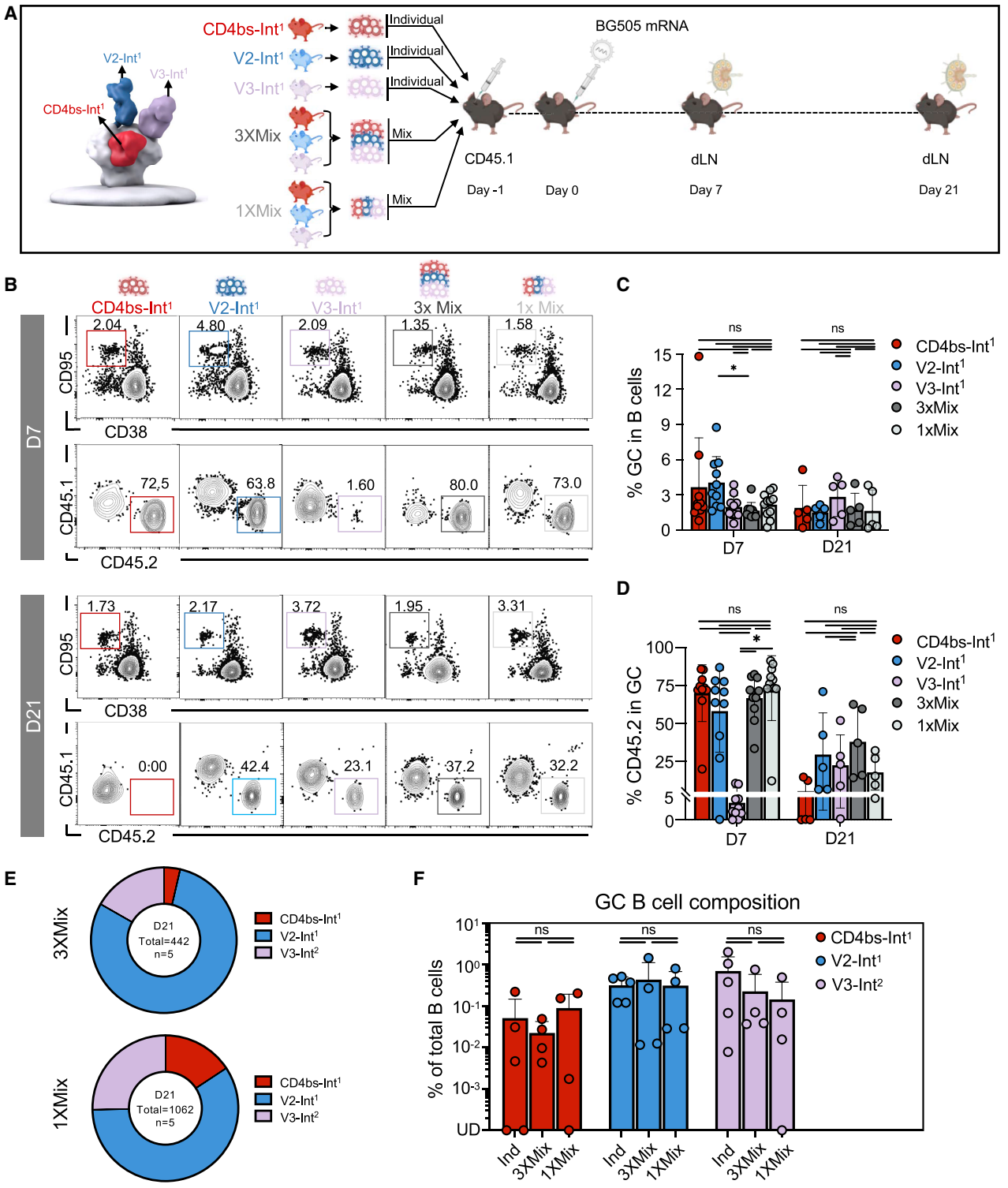


**Figure 2. A single trimer simultaneously activates intermediate B cells targeting V2-apex, V3-glycan, and the CD4bs in the same host**

(A) Schematic of individual- or co-adoptive-transfer and immunization experiments for CD4bs-Int$^1$, V2-Int$^1$, and V3-Int$^1$ B cells.

(B) Representative FACS plots of B cells obtained from dLNs after individual- or co-adoptive-transfer. Events pre-gated on lymphocytes/singlets/live/CD4$^-$CD8$^-$F4/80$^-$Gr1$^-$/B220$^+$ B cells and represent (upper) GC and (lower) CD45.2 cells in GC.

(C and D) Quantification of (C) GC cells as the percentage of total B cells and (D) CD45.2$^+$ cells as the percentage of GC B cells at D7 and day 21. *q* values were calculated by the Kruskal-Wallis test followed by pairwise comparisons with Benjamini-Krieger-Yekutieli (BKY) correction.

*(legend continued on next page)*

though LC frequencies varied by treatment (Figures S2C and S2D). The GC kinetics of each of the epitope-specific cell lines were thus unaffected by the presence of lines targeting non-overlapping epitopes on the same immunogen.

## B cell lines with low, comparable affinities to the same epitope can be costimulated

Although we did not observe inhibition among B cell lines targeting different epitopes on the same trimer, to explore possible crosstalk between lineages targeting the same epitope, we generated an additional mouse line using minBG18.11 (V3-Int$^2$), which targets the same V3-glycan epitope as minBG18.6 (V3-Int$^1$) but represents a more affinity-matured variant with higher SHM from germline.[40] Homozygous V3-Int$^2$ mice ($IgH^{minBG18.11/\ minBG18.11}Ig\kappa^{WT/WT}$) displayed normally developing B cells that could survive, proliferate, and differentiate *in vitro* (Figures S3A–S3C). BG505-specific PBMC frequency was 27.9%, similar to that observed in V3-Int$^1$ (Figures 1B, 1C, 3A, and S3D). As in the V3-Int$^1$ mouse line, the V3-Int$^2$ HC sequences also paired with a variety of endogenous murine LCs, most commonly IGKV12-46, IGKV12-41, IGKV10-94, IGKV4-50, and IGKV12-98 (Figure 3B). V3-Int$^1$ and V3-Int$^2$ displayed similar GC kinetics post-immunization by BG505 mRNA-LNP, with V3-Int$^2$ showing a slightly decreased GC size from 3.2% to 1.5% between day 14 and day 28. CD45.2$^+$ cells in GC were 35% at day 14 and 45% at day 28 (Figures 3C, 3D, S3E, and S3F). While V3-epitope recognition is strongly HC dependent,[40] the recombination with murine LCs adds further diversity, and the affinity of mAbs representative of V3-Int$^2$ BCRs to BG505 ranged from 1 μM to 10 μM, comparable to V3-Int$^1$ representative mAbs (Figure 3E).

To establish a repertoire of B cells targeting the same epitope, V3-Int$^2$ and V3-Int$^1$ CD45.2$^{+/+}$ B cells were adoptively transferred into CD45.1$^{+/+}$ host mice either individually, to reach a frequency of 20 cells per $10^6$ total B cells, or in equal-proportion combinations (mix) to reach a combined frequency of 40 per $10^6$. Recipients were intramuscularly (*i.m.*) immunized 1 day later (day 0) with BG505 mRNA-LNP, and local dLNs were analyzed at days 14 and 28 (Figure 3F). Mix-transfer recipients had larger GCs than either single-transfer group at day 14, but no significant differences were observed at day 28 (Figures 3G and 3H). The frequency of antigen-specific CD45.2$^+$ B cells in GCs increased over time. At day 28, CD45.2$^+$ B cells were slightly more frequent in GCs in the mix recipients compared with V3-Int$^2$ recipients, but frequencies were otherwise similar across groups at both time points (Figures 3G and 3H). CD45.2$^+$ cells from mix-transfer recipients were sorted for 10× scRNA-seq. Both V3-Int$^1$ and V3-Int$^2$ B cells were recovered at days 14 and 28 (Figures 3I and S3G). Upon multiplexing to GC CD45.2$^+$ percentages per mouse, no significant differences in relative B cell frequencies were observed between the single-transfer and the mix-transfer groups (Figures 3J and S3H). While V3-Int$^1$ HC isolated from mix recipients had higher SHM at day 14 than those from individual transfer groups, these differences equilibrated by day 28, and no differences were apparent in V3-Int$^2$ HC SHM across treatments (Figures 3K and S3I). V3-Int$^1$ HC maintained their preference for IGKV4-91, IGKV4-61, and IGKV4-50 LCs whether developing alone or accompanying V3-Int$^2$. Similarly, V3-Int$^2$ HC prefers IGKV12-46, IGKV4-50, and IGKV4-61 in both single and mixed transfer scenarios, though the frequencies of these most common pairings varied (Figure 3L). We observed no differences in class-switching profiles for either V3-Int$^1$ or V3-Int$^2$ B cells between individual and mix-transfer recipients (Figure S3J). Thus, despite engaging precisely the same epitope on the mRNA-LNP-delivered immunogen with overlapping affinity ranges, V3-Int$^1$- and V3-Int$^2$-derived B cells do not alter one another's GC participation or SHM accumulation.

## High-affinity B cells filter out lower-affinity cells targeting the same epitope

As V3-Int$^1$ and V3-Int$^2$ have variable affinities to BG505 with overlapping ranges, to clarify the effects of affinity on intra-epitope competition, we generated an additional HC+LC line targeting the CD4bs. We used the sequences of the Ab min12A21[53] to generate $IgH^{min12A21/min12A21}Ig\kappa^{min12A21/min12A21}$ (referred to as CD4bs-Int$^2$ below), which has lower levels of SHM than CD4bs-Int$^1$. The affinity of CD4bs-Int$^2$ to the BG505 trimer (46 nM) is lower than that of CD4bs-Int$^1$ (3 nM) (Figure 4A), though both are quite high compared with V3-Int$^1$ and V3-Int$^2$, which ranged between 1 and 10 μM (Figure 3E). An average of 31.2% of CD4bs-Int$^2$ PBMCs bound the BG505 probe (Figures 4B and S4A), and 10× scRNA-seq demonstrated that the BCRs of binders almost exclusively expressed the full-length CD4bs-Int$^2$ HC and LC sequences (95% HC and 97% LC), similar to CD4bs-Int$^1$ (Figures 4C and 1A). CD4bs-Int$^2$ development to follicular B cells, as well as survival, proliferation, and differentiation *in vitro*, were comparable to CD4bs-Int$^1$ (Figures S4B–S4D). Following stimulation with BG505 mRNA-LNP, CD4bs-Int$^2$ B cells could be recruited to GCs at day 7 and maintained, averaging 43% at day 7 and 29% at day 28 (Figure 4D). This contrasts sharply with CD4bs-Int$^1$ B cells, which were nearly undetectable in GCs at day 21 (Figure 1G).

After demonstrating a lack of inhibitory competition between V3 cells with low, overlapping-affinity ranges, the CD4bs-Int$^2$ and CD4bs-Int$^1$ KIs allow for the exploration of same-epitope B cells with high affinities differing by approximately 15-fold. CD4bs-Int$^1$ and CD4bs-Int$^2$ CD45.2$^+$ B cells were adoptively transferred into WT mice either individually (to achieve a frequency of 20 per $10^6$ total B cells) or in

(E) CD4bs-Int$^1$ (red), V2-Int$^1$ (blue), and V3-Int$^1$ (purple) B cell lineage frequency analysis from 10× scRNA-seq of GC CD45.2 B cells sorted at day 21 from the 3× mix (top) and 1× mix (bottom) groups. Pie charts are averages of all mice in a group (total = sequences amplified, *n* = mice).
(F) CD4bs-Int$^1$, V2-Int$^1$, and V3-Int$^1$ BCR composition of GC CD45.2 B cell sequences as percentages of total B cells at day 21. Percentage was calculated from FACS data for individual groups and from 10× scRNA-seq plus FACS data for mix groups. Values of zero on the $\log_{10}$ scale were plotted as UD. *q* values were calculated by the two-way ANOVA test followed by pairwise comparisons with BKY correction.
Figures represent data from one of at least two experiments with 3–5 mice per condition. Bars are mean + SD. Each dot represents one mouse. *q* values: $^*p < 0.05$, ns = not significant.
See also Figure S2.

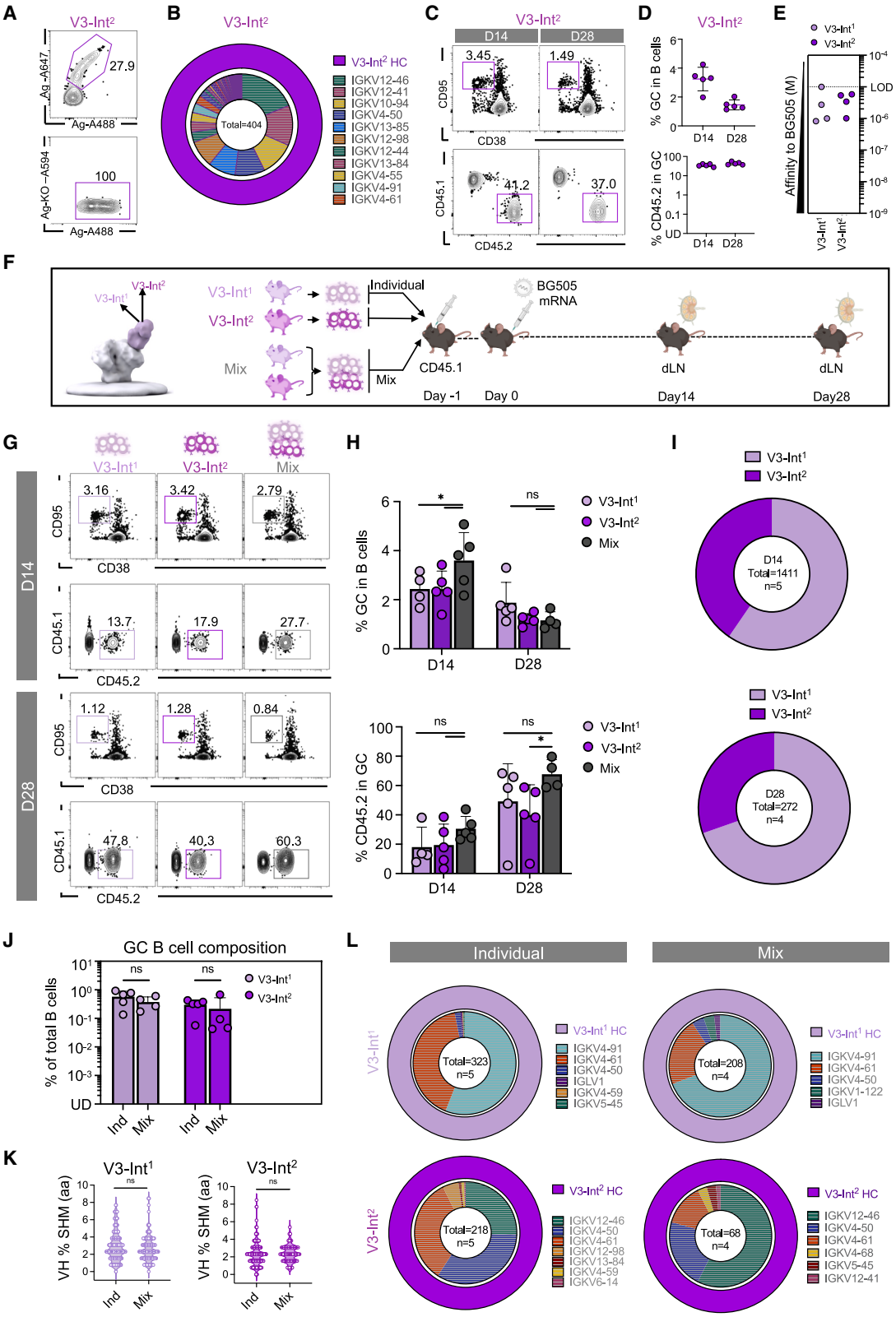


**Figure 3. Two B cell lineages targeting V3-glycan epitope can be simultaneously activated without competitive interference**

(A) Representative FACS plots of BG505-double-positive and BG505-epitope-specific KO-negative peripheral B cells in naive V3-Int$^2$ mice. Events were pre-gated on lymphocytes/singlets/CD4$^-$CD8$^-$F4/80$^-$Gr1$^-$/B220$^+$ B cells.

*(legend continued on next page)*

equal combination (combined frequency: 40 per $10^6$), and recipients were immunized with BG505 mRNA-LNP (Figure 4E). All groups displayed similar GC sizes (Figures 4F and 4G, upper). At day 7, CD45.2$^+$ B cell frequencies in GCs were comparable across single and mixed transfer recipients. By day 21, however, CD4bs-Int$^2$ B cells maintained high GC presence only when transferred individually, with significantly reduced frequencies observed when co-transferred with high-affinity CD4bs-Int$^1$ B cells (Figures 4F and 4G, lower). By contrast, the frequency of high-affinity CD4bs-Int$^1$ B cells in GCs decayed rapidly to nearly undetectable levels at day 21 in both single and mixed transfer recipients (Figures 4F and 4G, lower). Doubling the antigen dose did not rescue the CD4bs-Int$^2$ response (Figures 4E–4G).

In mix-transfer recipients, scRNA-seq of CD45.2$^+$ GC B cells revealed that the higher-affinity CD4bs-Int$^1$ B cells dominated GCs at both days 7 and 21 independent of administered antigen dose, with only ~5%–10% of CD45.2$^+$ GC B cells belonging to the CD4bs-Int$^2$ lineage (Figures 4H, S4E, and S4F). As above, we multiplexed the ratio to make the comparison per mouse and found a 1,000-fold decrease of CD4bs-Int$^2$ cells in GCs after the addition of CD4bs-Int$^1$. CD4bs-Int$^1$, by contrast, was unaffected by CD4bs-Int$^2$ (Figure 4I), demonstrating inhibition of CD4bs-Int$^2$ recruitment to or retention in GCs in the presence of CD4bs-Int$^1$. While CD4bs-Int$^2$ HC underwent lower rates of mutation in mixture recipients than when transferred alone, the CD4bs-Int$^1$ mutation rate was not affected by the presence of the low-affinity CD4bs-Int$^2$ line (46 nM) (Figure S4G). No differences in class-switch profiles were observed in either line (Figure S4H).

To determine whether competition for GC residence was mediated by inherent BCR affinity to the antigen, we generated a third CD4bs-targeting-bnAb-derived mouse line, $IgH^{N6\text{-}I2/N6\text{-}I2}$ $Ig\kappa^{N6\text{-}I2/\ N6\text{-}I2}$, referred to as CD4bs-Int$^3$, from another CD4bs-targeting Ab: N6-I2,[52] with affinity for the BG505 MD39 antigen ($K_D$, 5.7 nM) that was only slightly lower than the CD4bs-Int$^1$ affinity ($K_D$, 3 nM) (Figure S5A). Though CD4bs-Int$^3$, like CD4bs-Int$^1$, was less prevalent than CD4bs-Int$^2$ cells when transferred alone (Figures S5B–S5D), frequency within CD45.2$^+$ GC B cells was in order of descending affinity to BG505 in the triple mix (Figure S5E). The addition of CD4bs-Int$^3$ to the transfer mix did not affect the kinetics of CD4bs-Int$^1$ (Figure S5F), though greater SHM was observed in CD4bs-Int$^1$ (3 nM) after the addition of similarly high-affinity CD4bs-Int$^3$ (5.7 nM) cells in the triple mixture (Figure S5G). Thus, while no inhibition was observed among B cell lineages with comparable micromolar affinities targeting the V3-glycan supersite, same-epitope B cells with higher, nanomolar-range affinities targeting the CD4bs suppressed their lower-affinity counterparts.

## Lowering antigen affinity extends GC residence

The absence of CD4bs-Int$^2$ in later GCs in hosts also containing higher-affinity CD4bs-Int$^1$ cells (Figures 4F–4I), as well as the limited time in GCs for CD4bs-Int$^1$ after immunization (Figure 1F), led us to examine the effects of BCR affinity to the antigen on GC kinetics using protein immunization. We immunized mice transferred individually with CD4bs-Int$^1$ or CD4bs-Int$^2$ with BG505 protein adjuvanted with saponin/MPLA nanoparticles (SMNPs)[59] (Figures 5A and 5B). Day 8 GCs were similar after either transfer (2%–3%). GCs in lower-affinity CD4bs-Int$^2$ recipients peaked at day 16 at 6% and returned to 2% at day 21, while GCs in recipients of the higher-affinity CD4bs-Int$^1$ remained at 2.5% on day 16 before dropping to 0.7% on day 21 (Figures 5C and 5D). Within the GC, both CD4bs-Int$^1$ and CD4bs-Int$^2$ comprised approximately 6%–7% of GC B cells at D8, demonstrating successful recruitment. At day 16, however, GC occupancy rates of the lower-affinity CD4bs-Int$^2$ increased to approximately 12% and then to 16% on day 21. By contrast,

(B) Nested pie chart of human V3-Int$^2$ HC (purple), murine HC (gray), and murine LC sequences (multi-colored) amplified from single-cell sorted epitope-specific (BG505$^+$KO$^-$) naive B cells in V3-Int$^2$ mice. Legend shows the names of the most frequent 11 of 43 LCs amplified. Outer rings represent HCs, and inner rings represent LCs. Total = single cells amplified.
(C) Representative FACS plots of B cells obtained from dLNs in V3-Int$^2$ adoptively transferred mice at day 14 and day 28 after immunization with mRNA-LNP-encoded BG505. Events are pre-gated on lymphocytes/singlets/live/CD4$^-$CD8$^-$F4/80$^-$Gr1$^-$/B220$^+$ B cells and represent GC, CD45.2 cells in GC.
(D) Quantification of (C). Each dot represents one mouse. Bars are mean ± SD.
(E) Affinity measurement of V3-Int$^1$ and V3-Int$^2$ Ab against BG505 trimer measured by SPR dissociation constant. V3-Int$^1$ and V3-Int$^2$ Abs were expressed with human HC and representative murine LCs, and detailed sequences can be found in the key resources table. Each dot represents the mean of four technical replicates. Dotted line marks LOD. Data for V3-Int$^1$ reproduced from Figure 1D.
(F) Schematic of individual or co-adoptive-transfer and immunization experiments for V3-Int$^1$ and V3-Int$^2$ B cells.
(G) Representative FACS plots of B cells obtained from dLNs of mice V3-Int$^1$ and V3-Int$^2$ B cells at day 14 and day 28 after BG505. Events were pre-gated on lymphocytes/singlets/live/CD4$^-$CD8$^-$F4/80$^-$Gr1$^-$/B220$^+$ B cells and represent GC and CD45.2 cells in GC.
(H) (Upper) GC cells as a percentage of total B cells and (lower) CD45.2$^+$ cells as a percentage of total GC B cells at day 14 and day 28. Each dot represents one mouse. $q$ values calculated by two-way ANOVA with pairwise post hoc comparisons adjusted using BYK correction.
(I) The V3-Int$^1$ (light purple) and V3-Int$^2$ (dark purple) B cell lineage frequency analysis from 10× scRNA-seq of GC CD45.2 B cells sorted from the mix group. Pie charts are averages of all mice in a group (total = sequences amplified, $n$ = mice).
(J) V3-Int$^1$ and V3-Int$^2$ BCR composition of GC CD45.2 B cell sequences as a percentage of total B cells. Percentage was calculated from FACS data for individual groups and from 10× scRNA-seq plus FACS data for mix groups. Values of zero were plotted as UD on the $\log_{10}$ scale. $q$ values calculated by two-way ANOVA Kruskal-Wallis with pairwise post hoc comparisons adjusted using BYK correction.
(K) Dotted violin plot of HC amino acid mutations across all sites at day 28. Each dot represents an HC sequence from one B cell. Analyzed using Mann-Whitney's test.
(L) (Upper) Nested pie chart showing V3-Int$^1$ HC and LC usage from single-cell sorted CD45.2 B cells at day 28 from individual transfer and mix recipients. Outer ring, human V3-Int$^1$ IGHV; inner ring, murine IGKV. (Lower) Nested pie chart showing V3-Int$^2$ HC and LC usage as upper. Nested pie charts are averages of all mice in a group (total = sequences amplified, $n$ = mice).
(C), (D), (G), and (H) display representative data from one of at least two experiments with 3–5 mice per condition. Bars are mean ± SD in (H) and (J). Significance is indicated as *$p$ < 0.05, **$p$ < 0.01, ***$p$ < 0.001, ****$p$ < 0.0001; ns = not significant.
See also Figure S1.

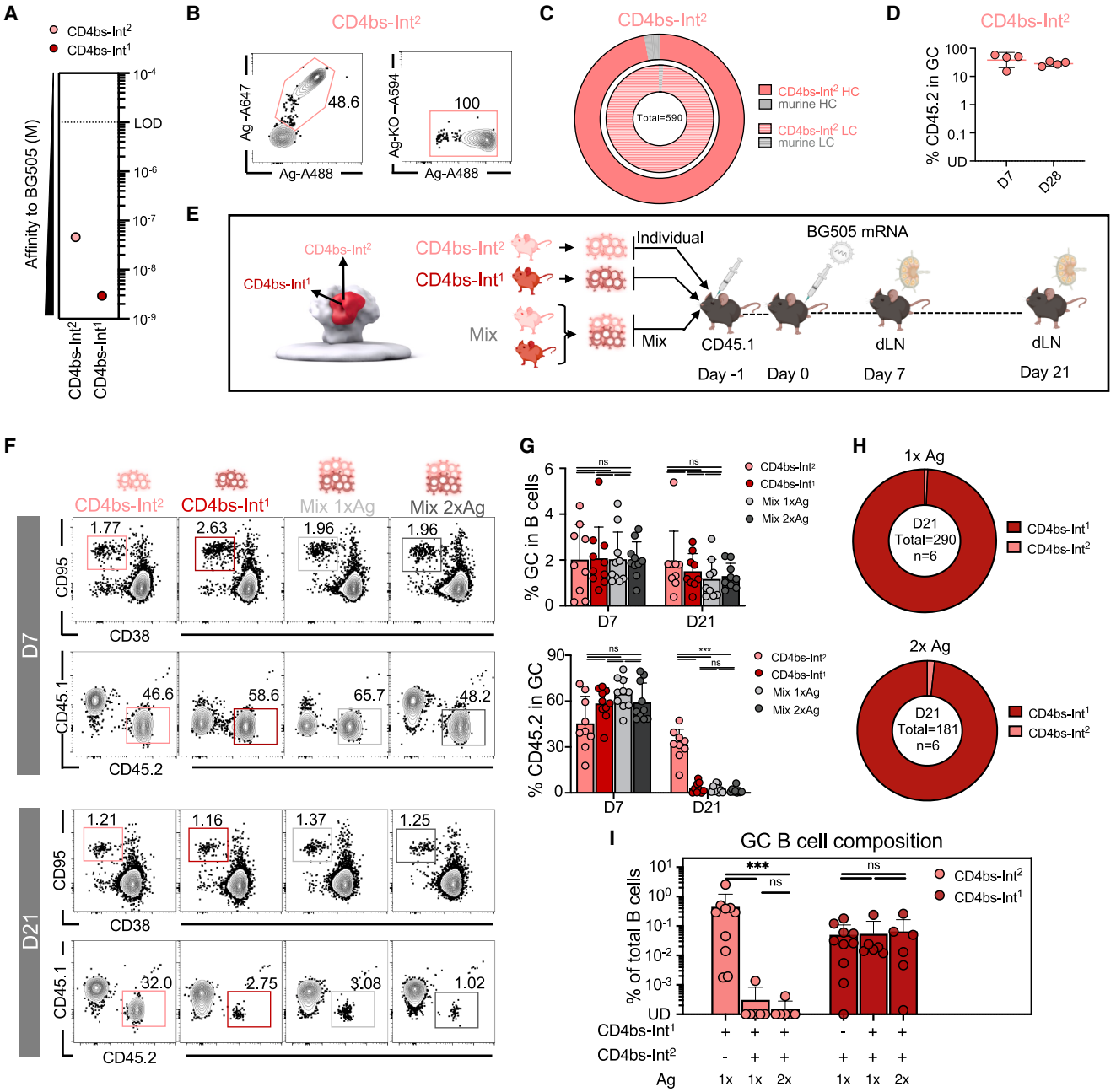


**Figure 4. Affinity-dependent inhibition of GC recruitment occurs between B cell lines competing for the CD4bs**

(A) Affinity of CD4bs-Int$^1$ and CD4bs-Int$^2$ human Ab against BG505 trimer measured by SPR dissociation constant. Each dot represents the mean of four technical replicates. Dotted line represents LOD.

(B) Representative FACS plots of BG505-double-positive and BG505-epitope-specific KO-negative peripheral B cells in naive CD4bs-Int$^2$ mice. Events were pre-gated on lymphocytes/singlets/CD4$^-$CD8$^-$F4/80$^-$Gr1$^-$/B220$^+$ B cells. Data are representative of ten total mice from five individual experiments.

(C) Nested pie chart of human CD4bs-Int$^2$ HC (shaded pink), murine HC (shaded gray), CD4bs-Int$^2$ LC (pink), and murine LC sequences (gray) amplified from single-cell sorted epitope-specific (BG505$^+$KO$^-$) naive B cells in CD4bs-Int$^2$ mice. Total = single cells amplified. Data produced from one representative of three mice.

(D) CD45.2$^+$ cells as a percentage of total GC B cells in dLNs of CD4bs-Int$^2$ adoptive transfer recipients at days 7 and 21 post-immunization by BG505. Values of zero were plotted as UD on the log$_{10}$ scale. Each dot represents one mouse. Bars are mean ± SD.

(E) Schematic of individual or co-adoptive-transfer and immunization experiments for CD4bs-Int$^1$ and CD4bs-Int$^2$ B cells. Recipient mice were adoptively transferred with either CD4bs-Int$^1$ or CD4bs-Int$^2$ B cells to reach a frequency of 20 in $10^6$ B cells before immunization with 2 μg of BG505 mRNA. Mice were sacrificed at day 7 and day 21.

(F) Representative FACS plots of B cells obtained from dLNs at day 7 and day 21 post-immunization by BG505 in individual or mix transfer recipients. Events were pre-gated on lymphocytes/singlets/live/CD4$^-$CD8$^-$F4/80$^-$Gr1$^-$/B220$^+$ B cells and represent GC, CD45.2 cells in GC.

*(legend continued on next page)*

by day 16 the higher-affinity CD4bs-Int$^1$ cells underwent a massive contraction to 0.4%, from which they did not recover on day 21 (Figures 5C and 5E).

To determine the effect of BCR affinity for different antigens on these kinetics, we then deployed another HIV protein trimer adjuvanted with SMNP, DU172 (Figures S6A–S6D), which displays lower affinity to both CD4bs-Int$^1$ ($K_D$, 13 nM for DU172 vs. 3 nM for BG505) and CD4bs-Int$^2$ ($K_D$, 375 nM for DU172 vs. 46 nM for BG505) (Figures 5F and 5G). Total GC sizes were similar in both lines throughout (~2%–5%) (Figures 5H and 5I). Strikingly, no significant difference in CD45.2 cell presence in GCs was observed between these lines (Figures 5H and 5J), despite the fact that the ratio of CD4bs-Int$^1$:CD4bs-Int$^2$ BCR affinities for DU172, or the "affinity gap," is 29.4-fold greater than their 15.6-fold affinity gap for BG505 (Figures 5B and 5G). Both CD4bs-Int$^1$ and CD4bs-Int$^2$ were present in GCs until day 21 (Figures 5H and 5J). Thus, with BG505 immunization, CD4bs-Int$^1$ and CD4bs-Int$^2$ were recruited to GCs at day 8 at equivalent rates, but the high-affinity CD4bs-Int$^1$ ($K_D$, 3 nM for BG505) B cells diminished by day 16 and were absent at day 21. By contrast, after immunization with the lower-affinity antigen DU172, both CD4bs-Int$^1$ and CD4bs-Int$^2$ remained in GCs out to day 21. Thus, lowering antigen affinity below the ~3–12 nM ceiling prolongs GC residence.

## Antibody-mediated epitope masking suppresses competing B cells in an affinity-dependent manner

Since B cells targeting the same epitope did not directly compete for antigen, while lower-affinity CD4bs-specific B cells were inhibited by CD4bs-Int$^1$ (Figures 4G–4I), we investigated whether epitope masking from secreted antibody after early fate determination could inhibit B cells from the same epitope. First, we established a model with higher-affinity passively transferred Abs and lower-affinity B cells targeting the same epitope (Figure 6A): CD45.2$^{+/+}$ B cells from CD4bs-Int$^2$ donor mice (46 nM affinity to BG505) were adoptively transferred into CD45.1$^{+/+}$ host mice through the retro orbital sinus (day –1). Approximately 8 h later (time point referred to as day –0.5), CD4bs-Int$^1$ Abs (3 nM affinity to BG505) were injected into host mice through the tail vein, and approximately 16 h later (day 0), recipient mice were immunized with BG505 mRNA. At day 10 post-immunization, dLNs were sampled for flow cytometry (Figure 6A). Although GCs formed and were a larger fraction of B cells at the higher mAb doses (3 and 30 μg), all CD4bs-Int$^1$ mAb doses higher than 0.05 μg diminished the percentage of CD4bs-Int$^2$ B cells in GCs substantially relative to a control mAb; 0.3 μg decreased CD4bs-Int$^2$ B cell participation from 14% to 3%; and at 3 and 30 μg, CD4bs-Int$^2$ B cells were almost entirely blocked from GCs (1% for 3 μg, 0.3% for 30 μg) (Figures 6B and 6C). Next, we repeated the passive transfer of CD4bs-Int$^1$ Ab followed by immunization in mice instead adoptively transferred with equivalently high-affinity CD4bs-Int$^1$ B cells (Figure 6D). GC size increases were not significant after mAb delivery, and no significant change in the proportion of CD4bs-Int$^1$ B cells in GCs was observed at 0.3 μg compared with the control group; however, near-total blocking was observed when the Ab dose was increased to 3 or 30 μg (Figures 6E and 6F). Thus, low concentrations (0.3 μg) of high-affinity CD4bs-Int$^1$ mAb were sufficient to inhibit lower-affinity CD4bs-Int$^2$ cells, but higher concentrations (3 μg and 30 μg) also inhibited cells of equivalent affinity for the antigen.

We then repeated both adoptive transfers with the lower-affinity CD4bs-Int$^2$ mAb ($K_D$, 46 nM for BG505) (Figures 6G and 6J). As before, high mAb doses increased GC size. While 0.05 μg had no effect, CD4bs-Int$^2$ mAb inhibited CD4bs-Int$^2$ B cells in GCs beginning at a dose of 0.3 μg and reached near-total inhibition at 3 and 30 μg (Figures 6H and 6I). By contrast, while high mAb doses also increased GC size, 0.3 μg of CD4bs-Int$^2$ mAb did not produce any significant decrease in CD4bs-Int$^1$ B cells in GCs. Higher doses of CD4bs-Int$^2$ Ab did reduce CD4bs-Int$^1$ B cell numbers in GCs, however (Figures 6K and 6L). Thus, antibody-mediated epitope masking suppresses GC participation in an affinity- and concentration-dependent manner, with feedback sensitivity governed by BCR affinity.

## Local PCs provide antibody feedback to GCs

To determine whether emerging PCs and subsequent antibody production could contribute to GC kinetics, we next interrogated PC populations in and around GCs. GC formation occurs 5–7 days post-immunization, and short-lived PCs arise early.[60] As the frequency of CD4bs-Int$^1$ B cells in GCs declined dramatically between day 7 and day 16 post immunization, we focused on days 6 to 9 to capture this transition. Mice were adoptively transferred with either CD4bs-Int$^1$ or CD4bs-Int$^2$ cells and then immunized with 8 μg BG505 mRNA, after which flow cytometry was used to evaluate both CD45.2 recruitment to GCs and differentiation into plasma-like (CD138$^+$) cells in and out of GCs in dLNs (Figure 7A). At day 6 to day 8, significantly more CD45.2$^+$ cells were recruited to GCs after CD4bs-Int$^1$ transfer compared with CD4bs-Int$^2$ transfer, but the difference was no longer apparent by day 9 (Figures 7B and 7C). Within GCs (inGC) at day 6, numbers of plasma-like (CD138$^+$) cells were similar for CD4bs-Int$^1$ (25%) and CD4bs-Int$^2$ (18%). At day 7 and day 8, CD138$^+$ CD45.2 B cells were significantly higher in CD4bs-Int$^1$ recipients (D7 = 24%; D8 = 15%) than CD4bs-Int$^2$ recipients (day 7 = 10%; day 8 = 1%), but by day 9, few or no cells remained in GCs in either model (CD4bs-Int$^1$ = 3.6%; CD4bs-Int$^2$ = 0%) (Figures 7B and 7C). In unimmunized control mice, dLN from mice adoptively transferred with CD4bs-Int$^1$ or CD4bs-Int$^2$ showed no detectable CD138$^+$CD45.2 cells in GCs

(G) (Upper) GC cells as a percentage of total B cells and (lower) CD45.2$^+$ cells as a percentage of total GC B cells at days 7 and 21.
(H) The CD4bs-Int$^2$ (pink) and CD4bs-Int$^1$ (red) B cell lineage frequency analysis from 10× scRNA-seq of GC CD45.2 B cells sorted from the mix groups at day 21. Pie charts are averages of all mice in a group (total = sequences amplified, *n* = mice).
(I) BCR composition of GC CD45.2 B cell sequences as a percentage of total B cells at day 21. Percentage was calculated from FACS data for individual groups and from 10× scRNA-seq plus FACS data for mix groups. Values of zero were plotted as UD on the $\log_{10}$ scale.
(G–I) present data pooled from 2 experiments of 3–5 mice per condition. Bars are mean ± SD in (G) and (I). Each dot represents one mouse. *q* values calculated by nonparametric Kruskal-Wallis test with pairwise post hoc comparisons adjusted using BYK correction: ***$p < 0.001$; ns = not significant.
See also Figure S4.

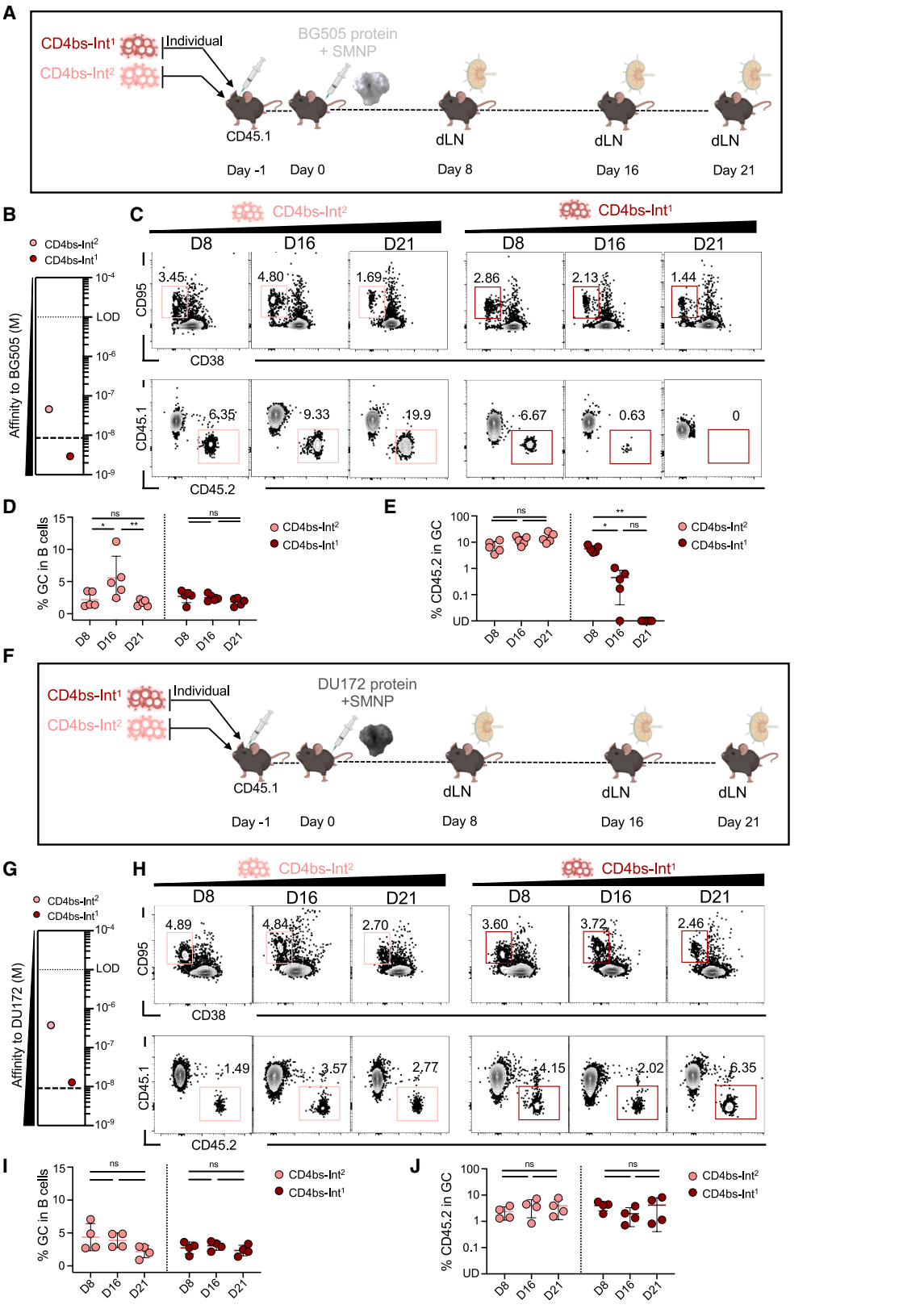


*(legend on next page)*

from D6-D9 (Figure S7B). In immunized mice, for local draining lymph node B cells not in GCs (exGC), the two lines were similar at D6 and highly divergent after that: CD4bs-Int$^1$ maintained ~40% of plasma-like CD138$^+$ cells exGC throughout. CD4bs-Int$^2$ CD138$^+$ cells exGC decreased from 25% at day 6 to 6.5% at day 9 (Figures 7B and 7C). The exGC environment thus contained detectable plasma-like cells from day 6 to day 9 for either line, but CD4bs-Int$^1$-derived PCs remained at far higher percentages. This group of plasma-like CD138$^+$ cells was also observed at day 8 inGC (9%) and exGC (30%) in CD4bs-Int$^1$ recipient mice but not CD4bs-Int$^2$ recipients after lower-affinity DU172 protein immunization. The population decreased below 1% between day 8 and day 16 (Figures S6E and S6F). The lower numbers of early CD138$^+$ cells in dLN, especially inGC, could be related to longer GC residence in lower-affinity DU172 immunization.

The observation of CD138$^+$ cells both inGC and exGC by flow cytometry pushed us to detail the spatial distribution of plasma-like cells in the dLN. To determine localization, we first deployed immunofluorescence (IF) staining in immunized mice adoptively transferred with either CD4bs-Int$^1$ (Figure 7D) or CD4bs-Int$^2$ (Figure S7C). dLN from mice adoptively transferred with CD4bs-Int$^2$ but left unimmunized were also examined as a control (Figure S7D). Nucleus staining for IRF4 was utilized for better visualization of plasma-like cell colocalization. Multiple GCs formed by D6 after BG505 immunization in the B cell follicles at the cortex of the dLN in adoptively transferred mice (Figures 7D and S7C). Some GCs were comprised almost entirely of CD45.2 cells. Of those CD45.2 cells within GCs, some were also positive for IRF4 nucleus staining, indicating that they were plasma-like; CD45.2 plasma-like (IRF4$^+$) cells were primarily observed in small groups at GC borders (Figures 7D and S7C). Using Slide-seq,[61,62] we then developed a whole-distribution map of plasma-like cells in dLN. Plasma-like cells, assigned by robust cell-type decomposition (RCTD)[63] using an immune scRNA-seq reference dataset,[64] were observed both within and around GCs, accumulating in the medullary cords, paracortex, or T-B border (Figures 7D, 7E, S7C, S7E, and S7F). Quantification of sufficiently sized GCs (≥100 beads) showed an average of 1.5 PCs per 100 GC cells in the inner GC core, 6.6 per 100 in the outer GC ring, and 20.3 per 100 in the 30 μm periphery of the GC (Figures S7G and S7H). Gene expression analysis found upregulation of Ab secretion-related genes, including secretion components (*Jchain*, *Ighg1*, *Ighg2b*, and *Ighg2c*), as well as protein folding machinery (*Calr*, *Pdia4*, and *Hspa5*), in PCs within the anatomical range of the GC relative to non-PC GC B cells. Expression by inGC PCs reached similar or slightly lower levels compared with PCs exterior to the GC (Figures 7F and S7I), suggesting potential Ab secretion functions in those cells.

To determine whether these PC populations in and around the GC produced Ab, dLNs from different time points were mechanically disrupted in buffer, and ELISA against BG505 was performed on the resulting supernatant. Based on prior measurements of murine LN volumes,[65–70] we estimated that a minimum of a 5× dilution occurs at the mechanical disruption stage; therefore, we applied a 5× correction to estimate endpoint titer in the dLNs. Compared with unimmunized mice adoptively transferred with the same CD45.2 cells, high titers of immunoglobulin G (IgG) were detected in dLNs at D6 to D9 after immunization. For CD4bs-Int$^2$, the estimated endpoint titer for dLN IgG increased from $3\times10^4$ at D6 to $1\times10^5$ at D7 to a peak of $2 \times 10^5$ at D8 and then dropped to $1\times10^4$ at D9. High-affinity CD4bs-Int$^1$ presented a higher and more stable dLN IgG titer curve above $8 \times 10^4$ from D6 to 9, with a slightly earlier peak of $2 \times 10^5$ at D7. At D7, a small BG505-CD4bs-KO probe peak was observed for CD4bs-Int$^2$ (at $5 \times 10^3$) and CD4bs-Int$^1$ ($8 \times 10^2$), potentially indicating a small amount of IgG produced by host mouse B cells targeting other epitopes (Figure 7G). Compared with IgG, IgM titers peaked at a lower level ($5 \times 10^3$) and early (by D6) in dLNs of both types of transfer recipients, with low-affinity CD4bs-Int$^2$ persisting until D9, while, by contrast, high-affinity CD4bs-Int$^1$ dropped at D7. No IgM was detected above the detection limit of 250 for either the CD4bs-Int$^1$- or CD4bs-Int$^2$-transferred unimmunized group or by BG505-CD4bs-KO probes (Figure S7J). The observation that neither IgG nor IgM was detected in the dLN of unimmunized

**Figure 5. Affinity-related GC kinetics of competing CD4bs-targeting precursor lines**

(A) Schematic of BG505 immunization experiments for CD4bs-Int$^1$ and CD4bs-Int$^2$ B cells. Mice were immunized with BG505 Env glycoprotein trimer protein with SMNP adjuvant.

(B) Affinity of CD4bs-Int$^1$ and CD4bs-Int$^2$ human Ab against BG505 trimer measured by SPR dissociation constant. Each dot represents the mean of 4 technical replicates. The dotted line represents LOD, and the dashed line proposes a potential affinity selection ceiling in our system in a low nanomolar range. Affinity data reproduced from Figure 4D for reference.

(C) Representative FACS plots of GC B cells obtained from dLNs after BG505 immunization at day 8, day 16, and day 21. Events were pre-gated on lymphocytes/singlets/live/CD4$^-$CD8$^-$F4/80$^-$Gr1$^-$/B220$^+$/GC B cells and represent CD45.2 cells in GC.

(D) Kinetics of GCs over time after BG505 immunization.

(E) Kinetics of CD45.2 cells in GCs over time after BG505 immunization. Values of zero were plotted as UD on the $\log_{10}$ scale.

(F) Schematic of DU172 immunization experiments for CD4bs-Int$^2$ and CD4bs-Int$^1$ B cells. Mice were immunized with DU172 Env glycoprotein trimer protein with SMNP adjuvant.

(G) Affinity of CD4bs-Int$^1$ and CD4bs-Int$^2$ human Ab against DU172 trimer measured by SPR dissociation constant. Each dot represents the mean of 4 technical replicates. Dotted line represents LOD, and the dashed line proposes the potential affinity selection ceiling in a low nanomolar range.

(H) Representative FACS plots of GC B cells obtained from dLNs after DU172 immunization at day 8, day 16, and day 21. Events were pre-gated on lymphocytes/singlets/live/CD4$^-$CD8$^-$F4/80$^-$Gr1$^-$/B220$^+$/GC B cells and represent CD45.2 cells in GC.

(I) Kinetics of GC B cells after DU172 immunization.

(J) Kinetics of CD45.2 cells as the percentage of GC B cells after DU172 immunization. Values of zero were plotted as UD on the $\log_{10}$ scale.

Panels show data from one representative experiment of at least two performed; 3–5 mice per condition. Dots represent single mice. Bars are mean ± SD. *q* values calculated by the nonparametric Kruskal-Wallis test followed by pairwise post hoc comparisons adjusted using BKY correction: $^*p < 0.05$, $^{**}p < 0.01$, ns = not significant.

See also Figure S6.

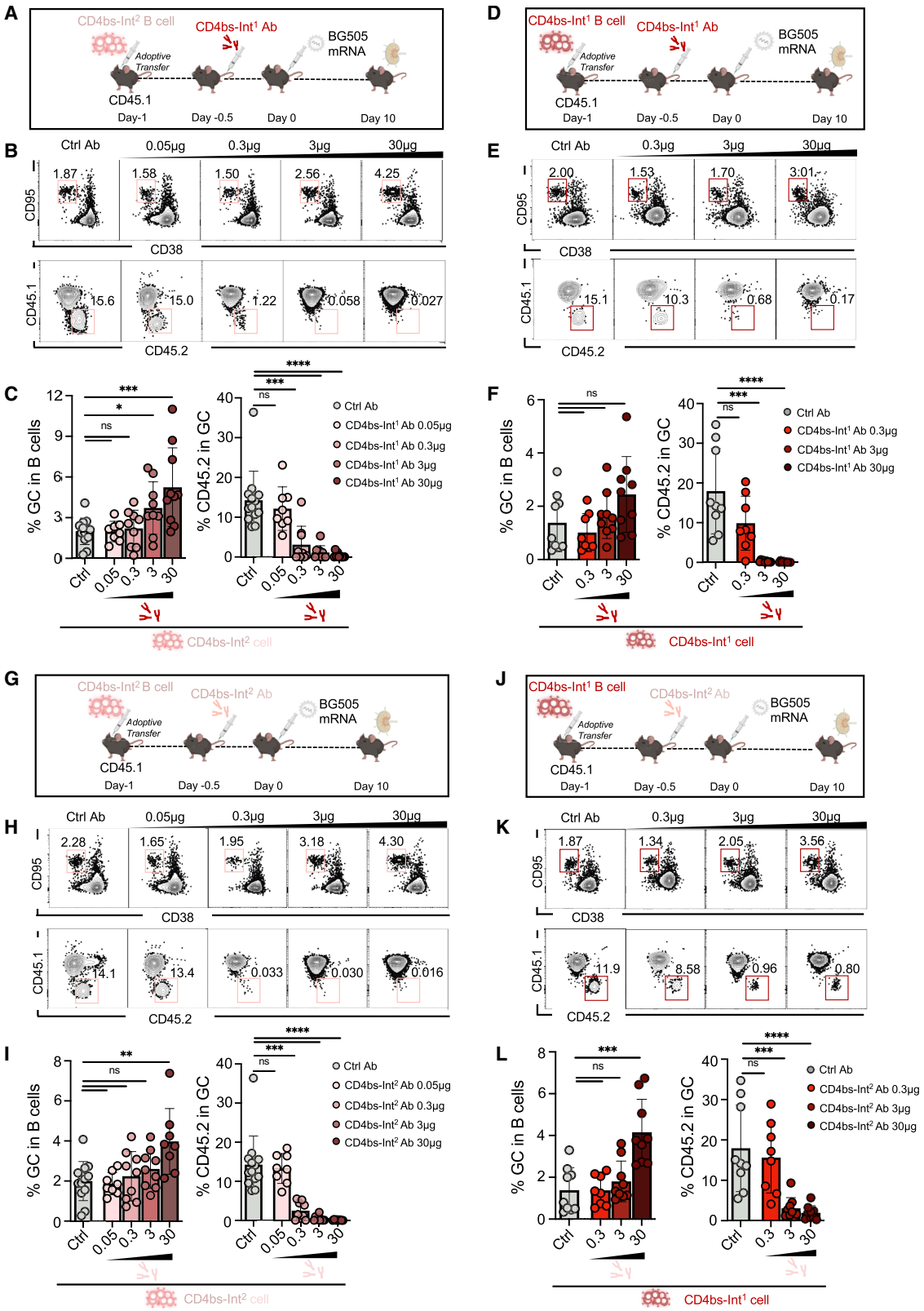


*(legend on next page)*

adoptive transfer recipients excludes the possibility of a base from self-reactivity (Figures 7G and S7J). Local dLN titers may be higher than those in circulation at early time points (Figure S7K). To more precisely establish the localization of Ab production to the dLN, we performed single-side immunization on recipient mice and compared LN homogenate from ipsilateral dLNs and the contralateral LNs (Figures 7H, 7I, and S7L). At D8, the ipsilateral dLNs showed markedly higher average IgG titers in both CD4bs-Int$^2$ recipient ($5.1 \times 10^4$) and the CD4bs-Int$^1$ recipient ($6.4 \times 10^4$), while the contralateral LNs showed much lower IgG titers just above LOD ($6 \times 10^2$ for CD4bs-Int$^2$; $1 \times 10^3$ for CD4bs-Int$^1$) (Figures 7I and S7L). This result suggests that early Ab feedback could be more local than systematic.

To determine the affinities of the early antibody pool, mutated BCR sequences from D7 GC B cells were expressed as IgG mAbs *in vitro* and tested for affinity against the BG505 trimer. In D7 GC, mAbs isolated from CD4bs-Int$^1$-transfer recipients had relatively high affinities, with $K_D$ values ranging from 3 to 19 nM and a median $K_D$ of 5 nM, while mAbs from CD4bs-Int$^2$ recipients had relatively lower affinities, with $K_D$ values ranging from 34 nM to 2.5 μM and a median $K_D$ of 85 nM (Figure S7M). This indicated a maintenance of at least a 10-fold overall affinity gap between the Ab reservoirs generated by these two lineages. In sum, high early PC and antibody abundance in dLNs demonstrate the existence of a local antibody feedback loop that rapidly tunes GC competition.

## DISCUSSION

The classical model of GC selection is Darwinian, with higher-affinity B cells progressively outcompeting lower-affinity clones for antigen and survival signals.[71] Our data reveal an additional layer of regulation in which antibody feedback shapes GC dynamics. Using mouse models with BCRs of defined affinities and epitope specificities to the same immunogen, we found substantial initial recruitment of both high- and low-affinity B cells, but only lower-affinity cells persisted in GCs. Persistence was not a fixed characteristic of particular B cell lines but depended on affinity for the presented immunogen. Importantly, B cells targeting the same epitope with similar affinities could be costimulated without changing their individual GC residency patterns, whereas high-affinity clones suppressed lower-affinity counterparts. Spatial transcriptomics revealed the presence of PCs near GCs as a probable source of local secreted antibody and feedback mediating this suppression. Together, these findings suggest that antibody feedback may provide a critical regulatory "brake," enforcing affinity thresholds that shape B cell selection and exit from GCs, while also promoting epitope spreading as lower-affinity clones to other epitopes are not suppressed. This dual mechanism suggests vaccine strategies aiming to balance breadth and potency may need to modulate affinity and feedback dynamics.

B cells must meet a minimum affinity-to-antigen "floor" to enter GCs for affinity maturation.[3,5,11,12,72–74] As affinity increases, selective pressure on antigen-BCR binding may decrease.[3,18,19] Though high-affinity variants may still emerge, an affinity ceiling exists above which comparative selective advantage is lost. In the classic hapten-based system, B cells with higher initial BCR affinities to antigen accumulate fewer $V_H$ mutations than lower-affinity counterparts despite similar mutation rates, due to either relaxed positive selection or negative selection, as mutations in high-affinity BCRs may be likelier to diminish affinity.[13] In our real-world HIV-trimer-based system, similarly, only high-affinity competitors but not low-affinity competitors increased SHM rates in counterpart high-affinity cells, potentially due to positive selection. Antibodies produced by those first activated B cells can modulate this selective process by directly competing for antigen or inducing apoptosis in lower-affinity B cells.[25] High-affinity antibodies may be induced quite early, without affinity maturation.[19] Recent studies have highlighted the blocking effect injected high-affinity Abs can exert on immune responses.[27,28] In agreement with these studies, our findings suggest an Ab-driven self-modulation loop acts as a brake, reinforcing the upper affinity maturation ceiling in GCs. Notably, this brake is an intra-epitope phenomenon reproducible by passive antibody administration, suggesting that epitope masking by early antibody production may drive this system. The brake's epitope-specificity is congruent with

**Figure 6. Affinities and concentrations of antibodies competing for the same epitope determine GC response**

(A) Schematic of CD4bs-Int$^1$ Ab blocking experiments for CD4bs-Int$^2$ B cells.

(B) (Upper) Representative FACS plots of GC CD4bs-Int$^2$ CD45.2 B cells obtained from dLNs after CD4bs-Int$^1$ Ab pre-injection and BG505 mRNA immunization. Events were pre-gated on lymphocytes/singlets/live/CD4$^-$CD8$^-$F4/80$^-$Gr1$^-$/B220$^+$ B cells and represent GC in B cells. (lower) Representative FACS plots of CD45.2 B cells. Events were pre-gated on lymphocytes/singlets/live/CD4$^-$CD8$^-$F4/80$^-$Gr1$^-$/B220$^+$/CD38$^-$CD95$^+$ B cells and represent CD4bs-Int$^2$ CD45.2 cells in GC.

(C) (Left) GC B cells as a percentage of total B cells and (right) CD45.2$^+$ CD4bs-Int$^2$ cells as a percentage of GC B cells at D10.

(D) Schematic of CD4bs-Int$^1$ Ab blocking experiments for CD4bs-Int$^1$ B cells.

(E) Representative FACS plots of GC CD4bs-Int$^1$ CD45.2 B cells obtained from dLNs at day 10. Gated as in (B).

(F) (Left) GC B cells as a percentage of total B cells and (right) CD45.2$^+$ CD4bs-Int$^1$ B cells as a percentage of GC B cells at day 10.

(G) Schematic of CD4bs-Int$^2$ Ab blocking experiments for CD4bs-Int$^2$ B cells.

(H) Representative FACS plots of GC CD4bs-Int$^2$ B cells obtained from dLNs after CD4bs-Int$^2$ Ab pre-injection. Gated as in (B).

(I) (Left) GC B cells as a percentage of total B cells and (right) CD45.2$^+$ CD4bs-Int$^2$ B cells as a percentage of total GC B cells at day 10. Control group reproduced from (C).

(J) Schematic of CD4bs-Int$^2$ Ab blocking experiments for CD4bs-Int$^1$ B cells.

(K) Representative FACS plots of GC CD4bs-Int$^1$ B cells obtained from dLNs after CD4bs-Int$^2$ Ab pre-injection. Gated as in (B).

(L) (Left) GC B cells as a percentage of total B cells and (right) CD45.2$^+$ CD4bs-Int$^1$ B cells as a percentage of total GC B cells at day 10. Control group reproduced from (F).

30 μg of irrelevant flu MEDI8852 Ab was pre-injected to each mouse in all ctrl Ab groups. Figures represent data pooled from two experiments with 3–5 mice per condition. Each dot represents one mouse. Bars are mean + SD. *q* values calculated using the Kruskal-Wallis test followed by pairwise comparisons with BKY correction: $^*p < 0.05$, $^{**}p < 0.01$, $^{***}p < 0.001$, $^{****}p < 0.0001$; ns = not significant.

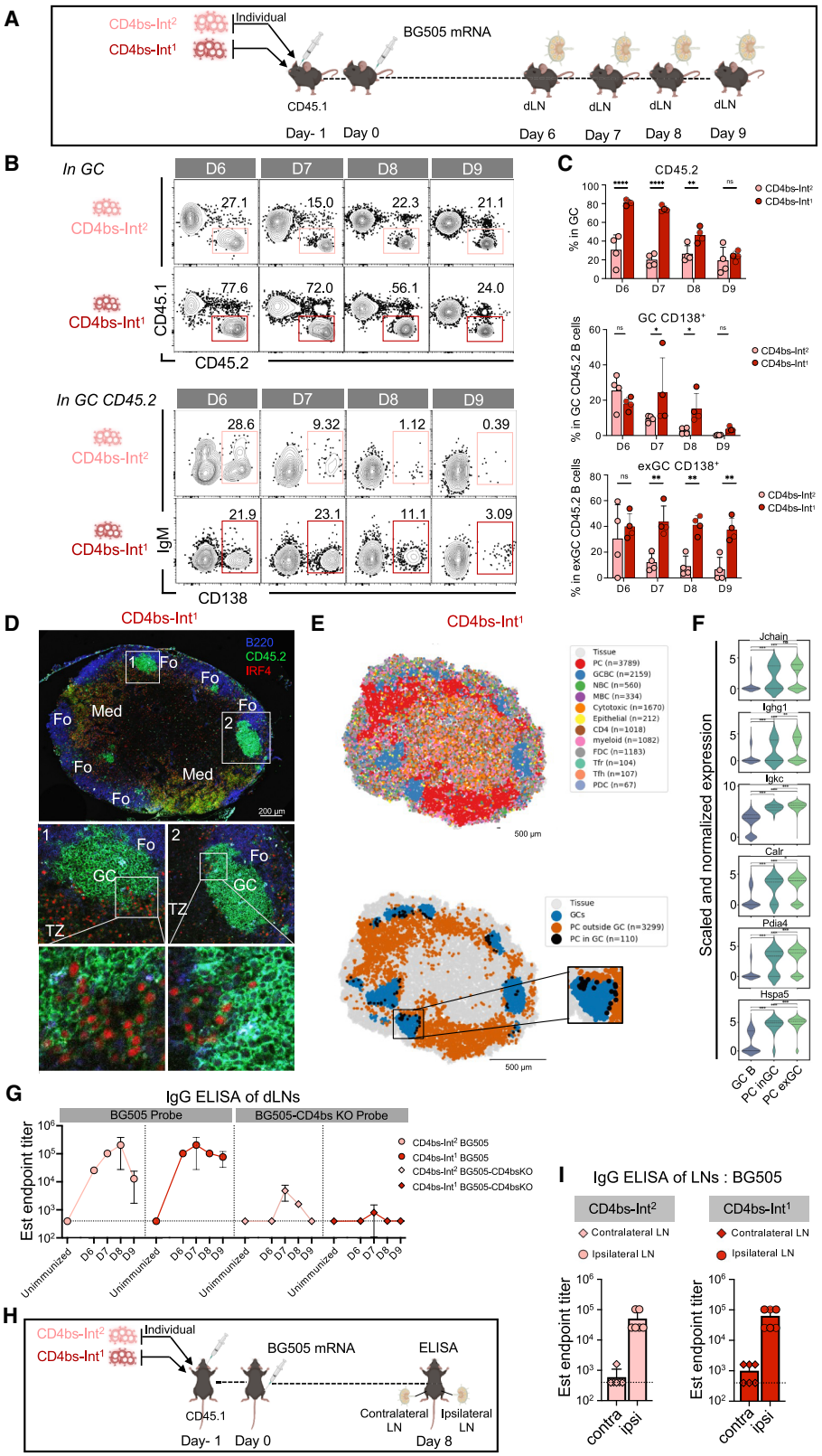


**Figure 7. PCs in and adjacent to GCs produce a local Ab pool that adjusts the GC response**

(A) Schematic of PC experiments. Recipient mice were adoptively transferred with either CD4bs-Int$^1$ or CD4bs-Int$^2$ B cells to reach a frequency of 50 in $10^6$ B cells before immunization with 8 μg of BG505 mRNA. Mice were sacrificed at D6, D7, D8, and D9.

*(legend continued on next page)*

recent findings in an influenza infection model, where affinities from interclonal PC differed by factors of a thousand or more, while intraclonal PCs only differed by factors of 10 to 30.[17] An intraclonal ceiling effect produced by Ab braking may drive GC B cell diversity and subdominant responses observed by multiple studies.[28–30,75–77] Interestingly, feedback from serum Abs has been observed not only hindering but also enhancing responses.[27–29,78] The increase in total GC sizes after high doses of Ab in our passive transfer experiments is suggestive of enhancement and is notable in light of recent work suggesting that Abs can essentially adjuvant mRNA-LNP immunization.[28] In contrast to the brake, Ab-driven self-modulation may also serve as the intra-epitope "filter" to exclude low-affinity lines from GC entry or residence—though avidity effects may rescue some low-affinity B cell GC participation.[79] Thus, initial BCR affinity to antigen and the timing of high-affinity Ab secretion may establish a self-modulating loop in which the brake drives diversity while the filter drives potency.

Much of our understanding of Ab feedback relates to circulating Ab titers and affinities.[27,28,76,80] By contrast, our observations of early Ab titer in dLN and PC in and around the GC suggest that a local, real-time PC-driven feedback loop determines B cell composition in primary GCs. Plasma fate commitment occurs in the light zone (LZ) with the upregulation of *Irf4*.[16,81–83] Immunofluorescent staining using single markers, such as IRF4, BLIMP1, CD138, or cytosol IgG1, had placed PC precursors predominantly in the T-B border, with rare subsets in the GC.[81,82,84,85] Gene expression of plasma-like cells (IRF4$^{-+}$), defined as GC-resident on the basis of CD38$^{-}$Fas$^{+}$, is similar to that of the total plasma-like population (CD138$^{+}$TACI$^{-}$).[86] Our Slide-seq data confirm the anatomical localization of inGC PCs designated by a comprehensive gene signature. Similar levels of upregulation of secretion components and protein folding machinery in inGC and exGC PCs imply inGC PC Ab secretion. Recent observations of unusually low extracellular protease levels inside B cell follicles in mouse LN[87] further support the possibility of a local Ab pool. Like the GC response itself, post-GC PC proliferation is affinity-dependent,[88] and our own observations suggest more inGC PCs from higher-affinity lines were present early. Thus, alongside precursor frequency, Ag affinity, and Ag avidity,[89] localized PC populations may determine GC kinetics by producing a local high-affinity secreted Ab pool.

Affinity- and kinetics-driven competition and Ab feedback have substantial implications for the vaccine-mediated development of breadth, particularly in contexts where the maturation of multiple B cell lineages is driven by the same immunogens to achieve broad neutralization, such as HIV sequential immunization.[32,39,41,90–92] While progress has been made in simultaneously priming diverse bnAb precursors,[93,94] little is known about how crosstalk between minimally matured antibodies and B cells will impact late-stage boosting strategies. The lack of inter-epitope B cell competition in our assays indicates that the brake on intra-epitope B cell development may be essential to a multi-epitope response. Where long GC reactions are preferable, the use of lower-affinity immunogens may release the self-braking mechanism. Furthermore, antigen affinity to the broader Ab and B cell repertoire must be considered. Though not ascribed to antibody production, the presence of higher-affinity non-precursor same-epitope responses has been observed as a limiting factor in B cell GC residence.[12] BnAb development strategies involving sequential immunization should identify functional affinity ranges for each immunization stage. A related concept, that the "affinity drop" between sequential antigens

(B) (Upper) Representative FACS plots of CD45.2 B cells. Events were pre-gated on lymphocytes/singlets/live/CD4$^{-}$CD8$^{-}$F4/80$^{-}$Gr1$^{-}$/B220$^{+}$/CD38$^{-}$CD95$^{+}$ B cells and represent CD45.2 B cells in GCs. (Lower) Representative FACS plots of plasma-like cells. Events were pre-gated on lymphocytes/singlets/live/CD4$^{-}$CD8$^{-}$F4/80$^{-}$Gr1$^{-}$/B220$^{+}$/CD38$^{-}$CD95$^{+}$/CD45.1$^{-}$CD45.2$^{+}$ B cells and represent plasma-like cells among GC CD45.2 B cells.
(C) (Upper) CD45.2$^{+}$ B cells as a percentage of GC B cells, (middle) CD138$^{+}$ cells as a percentage of GC CD45.2 B cells, and (bottom) CD138$^{+}$ cells as a percentage of exGC CD45.2 B cells at D6, D7, D8, and D9. Dots are individual mice, and bars are mean + SD. *q* values calculated by two-way ANOVA with pairwise post hoc comparisons adjusted using BYK correction.
(D) Representative immunofluorescent staining of dLN isolated from mice transferred with CD4bs-Int$^{1}$ B cells at D6 post-immunization by BG505, staining with B220 (blue, surface), CD45.2 (green, surface), and IRF4 (red, nucleus). Large tile presents an overview of the architecture of the whole LN; inset boxes present individual GCs and subsets of PCs in GC. Fo, follicle; MC, medullar cords; TZ, T cell zone. Scale bar, 200 μm.
(E) Slide-seq spatial map of dLN isolated from mice with CD4bs-Int$^{1}$ B cells D6 post-immunization by BG505. Mapping of dLN is (upper) colored by cell type annotations from gene expression profiles or (lower) colored by anatomical location in GC or exGC. Plasma cells (PCs), GC B cells (GCBCs), naive B cells (NBCs), memory B cells (MBCs), cytotoxic T cells (cytotoxic), epithelial cells (epithelial), CD4 T cells (CD4), follicular dendritic cells (FDCs), follicular regulatory T cells (Tfr), follicular helper T cells (Tfh), and plasmacytoid dendritic cells (PDCs). n = subset cells. Non-serial sections of the same dLN were used as in (D). Scale bar, 500 μm.
(F) Violin plots of expression level of genes related to Ab secretion in GCBCs and PCs in and out of GC by anatomical location in the dLN at D6. Pairwise group comparisons were performed using two-sided Mann-Whitney U tests, followed by Holm-Bonferroni correction. Statistical comparison for gene expression was only assessed up to $p < 0.001$.
(G) ELISA quantification of BG505-binding (circle) and BG505-CD4bs-KO-binding (diamond) IgG from 100 μL of dLN homogenates of CD4bs-Int$^{1}$ (red) or CD4bs-Int$^{2}$ (pink) recipient mice immunized with BG505 mRNA or left unimmunized. A 5× dilution multiplier was applied to obtain the final estimated (est) endpoint titer of dLNs. Dots represent mean values of technical triplicates from homogenates generated from one popliteal LN from each of the four mice pooled at D7, D8, and D9. Unimmunized dots include all data collected in groups left unimmunized after corresponding adoptive transfers. Dotted lines represent LOD.
(H) Schematic of single-side immunization experiment for CD4bs-Int$^{1}$ and CD4bs-Int$^{2}$ B cells. Recipient mice were adoptively transferred with CD4bs-Int$^{1}$ or CD4bs-Int$^{2}$ B cells, respectively, to reach a frequency of 50 in $10^{6}$ B cells before immunization with 8 μg of BG505 mRNA. Mice were sacrificed at D8 for ipsilateral dLNs and contralateral LNs as controls.
(I) ELISA quantification of BG505-binding IgG from 100 μL of dLN homogenates of ipsilateral dLNs (circle) and contralateral LNs (diamond) of CD4bs-Int$^{1}$ (red) or CD4bs-Int$^{2}$ (pink) recipient mice immunized with BG505 mRNA or left unimmunized. A 5× dilution multiplier was applied to obtain the final est endpoint titer of dLNs. For each group, homogenates were generated from one popliteal LN from each of the four mice pooled into 100 μL of buffer. Technical triplicates were performed for each group. Dots represent individual values pooled from two experiments. Bars are mean ± SD. Dotted lines represent LOD.
Significance is indicated as *$p < 0.05$, **$p < 0.01$, ***$p < 0.001$, ****$p < 0.0001$; ns = not significant.
See also Figure S7.

should not be too high or too low, was previously described, though also not ascribed to antibody production.[39]

In sum, our study elucidated a multi-faceted Ab feedback loop in B cell competition for the same immunogen, which served as a self-modulating affinity-dependent brake for development of B cell lineages to the same epitope, as well as a filter excluding lower-affinity B cells, while preserving a parallel evolutionary path for lineages to other epitopes. The use of vaccine models applicable to preclinical development provides direct applications to fine-tuning vaccine strategies to avoid inhibitory antibody feedback.

## Limitations of the study

Our findings demonstrate that inherent affinity affects the durability and magnitude of GC B cell responses. While we found antibody feedback compelling based on multiple lines of evidence, more direct tests using antibody-production-deficit B cells, such as *Blimp-1* knock-outs, remain for future investigations. Additionally, Slide-seq, while a powerful approach, has a lower capture rate than traditional RNA sequencing. As to our model system, where cross-epitope comparisons are made, we should note that the bnAbs used in our BCR transgenic mice differ in binding stoichiometry (monovalent vs. trivalent), binding modality (HCDR3 vs. $V_H$-gene dominant), approach geometry, and epitope composition. Binding stoichiometry and approach geometry may influence BCR crosslinking on antigen-decorated surfaces, while binding modality and epitope composition could affect BCR clustering. In particular, signaling thresholds may differ for BCRs recognizing predominantly proteinaceous epitopes from those engaging carbohydrate-rich epitopes, as glycan-mediated interactions may exhibit distinct binding kinetics or activation dampening via CD22 interactions.[95] Finally, the membrane-anchored presentation of the immunogen used here may be subject to quite different modulating forces than a soluble immunogen,[57,58,96] though no obvious differences in individual kinetics were observed in our soluble protein experiments. Overall, however, consistent affinity-dependent effects were observed both when varying BCR affinity through the generation of transgenic mouse lines expressing sequences from distinct bnAb precursors and when varying antigen affinity through different immunogens.

## RESOURCE AVAILABILITY

### Lead contact

Requests for further information and resources should be directed to and will be fulfilled by the lead contact, Facundo D. Batista (fbatista1@mgh.harvard.edu), except where noted otherwise below.

### Materials availability

Model animals and antibodies minBG18.6-1, minBG18.6-2, minBG18.6-3, minBG18.6-4, minBG18.11-1, minBG18.11-2, minBG18.11-3, minBG18.11-4, N6-I3-D7-1, N6-I3-D7-2, N6-I3-D7-3, N6-I3-D7-4, N6-I3-D7-5, N6-I3-D7-6, N6-I3-D7-7, N6-I3-D7-8, N6-I3-D7-9, Min12A21-D7-1, Min12A21-D7-2, Min12A21-D7-3, Min12A21-D7-4, Min12A21-D7-5, Min12A21-D7-6, Min12A21-D7-7, Min12A21-D7-8, and Min12A21-D7-9 are available from the corresponding author (F.D.B.) on request, under a standard material transfer agreement (MTA) with Massachusetts General Hospital. Plasmids or recombinant proteins for immunogens and sort reagents related to BG505 MD39.3 and DU172 MD39.2; antibodies 12A21, min12A21, N6-I2, N6-I3, N6, and PCT64-18D; or SPR reagents in this study are available from W.R.S. under an MTA with the Scripps Research Institute. mRNA-LNP vaccine construct for BG505 MD39.3 can be made available from S.H. if the recipient and Moderna are able to agree upon the terms of an MTA.

### Data and code availability

Slide-seq data have been deposited on the Broad Institute Single Cell Portal, and the repository URL is listed in the key resources table (https://singlecell.broadinstitute.org/single_cell/). Custom code used for analysis has been deposited on GitHub, and the repository URL is listed in the key resources table (https://github.com/). BCR sequences have been deposited to Zenodo, and the identifier DOI is listed in the key resources table (https://zenodo.org/).

## ACKNOWLEDGMENTS

We would like to thank all members of the Batista lab for experimental help, as well as the Ragon Flow Cytometry Core and Scientific Editing Platform. We would also like to thank the Irvine lab (Scripps) for the provision of SMNP. Funding was provided by the Gates Foundation Collaboration for AIDS Vaccine Discovery (CAVD) grants INV009585 and INV046626 (to F.D.B.); NAC INV-007522, INV-008813, and INV-034657 (to W.R.S.); the National Institute of Allergy and Infectious Diseases (NIAID) UM1 AI144462 (Scripps Consortium for HIV/AIDS Vaccine Development) (to W.R.S. and F.D.B.); the IAVI Neutralizing Antibody Center (NAC) to W.R.S.; and flexible funding from the Ragon Institute of Mass General Brigham, MIT, and Harvard (to F.D.B.). R.H.L. is supported by the National Science Foundation Graduate Research Fellowship.

## AUTHOR CONTRIBUTIONS

Y.Y. designed, planned, and performed experiments; analyzed and interpreted the data; and wrote the paper. X.W. contributed to the design and conduct of experiments. Z.X. coordinated sample processing and cell sorting. D.L.V.B. designed immunogens and antibodies, performed SPR analysis, and edited the paper. R.H.L. performed and analyzed section staining and Slide-seq. K.M.M. and C.A.C. designed antibodies and probes. J.M. Steichen designed immunogens and antibodies. L.X. assisted with confocal and *in vitro* stimulation experiments and mouse colony management. P.M.V. assisted with peritoneal lavage and FACS recording. M.A. and J.-H.K. provided antibodies. J.M. Shen reviewed the paper. A.V. performed section staining and Slide-seq. O.K. performed SPR. J.D.A. performed glycan profiling. A.A.A. assisted in sorting experiments. A.A. assisted in sample processing. B.C. assisted with spatial transcriptomic analyses. E.G., N.A., N.P., and R.T. purified immunogens and probes. J.R.E.-P. and Q.A.P. generated mouse lines. H.N. assisted in mice genotyping and breeding. A.E. assisted in affinity experiments. B.K. performed 10× sequencing. M.K. expressed immunogens and mAbs and purified mAbs. A.L. performed SPR. T.P. assisted in animal experiments. D.L. expressed immunogens and mAbs. S.E. expressed immunogens and mAbs. X.L. managed mouse colonies and lab resources. J.E.W. performed and analyzed 10× sequencing experiments. S.R.W. assisted in manuscript drafting and editing. S.H. produced mRNA-LNP vaccine constructs. M.C. performed glycan profiling. U.N. oversaw and performed mouse line generation. S.L., W.R.S., and F.D.B. conceived of and oversaw projects.

## DECLARATION OF INTERESTS

F.D.B. has consultancy relationships with Adimab, Third Rock Ventures, and *The EMBO Journal* and founded BliNK Therapeutics. W.R.S., S.H., and A.C. are employees of Moderna Inc. C.A.C., A.L., J.M.S., and W.R.S. are inventors on a patent for membrane-bound HIV Env trimer immunogens (Modified immunogenic proteins, US20230190914A1).

## DECLARATION OF GENERATIVE AI AND AI-ASSISTED TECHNOLOGIES

During the preparation of this work, the authors used ChatGPT in order to edit and improve the readability of some text. After using this tool, the authors reviewed and edited the content as needed and take full responsibility for the content of the published article.

## STAR★METHODS

Detailed methods are provided in the online version of this paper and include the following:

- KEY RESOURCES TABLE
- EXPERIMENTAL MODEL AND SUBJECT DETAILS
- METHOD DETAILS
  - Immunogen and probe design
  - Immunogen, probe, and Ab production
  - Bio-layer interferometry (BLI)
  - Site-specific glycan profiling
  - Surface Plasma Resonance (SPR)
  - B cell in vitro stimulation assay
  - Adoptive transfer and immunization
  - Flow cytometry and cell sorting
  - Single-cell BCR sequencing
  - LN homogenization and Enzyme-linked immunosorbent assays (ELISA)
  - Immunofluorescence and histology
  - Spatial transcriptomics: sample processing
  - Spatial transcriptomics: data analysis
  - Statistical analysis

## SUPPLEMENTAL INFORMATION

Supplemental information can be found online at https://doi.org/10.1016/j.immuni.2026.01.011.

Received: May 29, 2025
Revised: October 24, 2025
Accepted: January 7, 2026
Published: February 13, 2026

## REFERENCES

1. Eisen, H.N., and Siskind, G.W. (1964). VARIATIONS IN AFFINITIES OF ANTIBODIES DURING THE IMMUNE RESPONSE. Biochemistry *3*, 996–1008. https://doi.org/10.1021/bi00895a027.
2. Jerne, N.K. (1951). A study of avidity based on rabbit skin responses to diphtheria toxin-antitoxin mixtures. Acta Pathol. Microbiol. Scand., Suppl. *87*, 1–183.
3. Batista, F.D., and Neuberger, M.S. (1998). Affinity dependence of the B cell response to antigen: a threshold, a ceiling, and the importance of off-rate. Immunity *8*, 751–759. https://doi.org/10.1016/s1074-7613(00)80580-4.
4. Paus, D., Phan, T.G., Chan, T.D., Gardam, S., Basten, A., and Brink, R. (2006). Antigen recognition strength regulates the choice between extrafollicular plasma cell and germinal center B cell differentiation. J. Exp. Med. *203*, 1081–1091. https://doi.org/10.1084/jem.20060087.
5. Mesin, L., Ersching, J., and Victora, G.D. (2016). Germinal Center B Cell Dynamics. Immunity *45*, 471–482. https://doi.org/10.1016/j.immuni.2016.09.001.
6. Crotty, S. (2019). T Follicular Helper Cell Biology: A Decade of Discovery and Diseases. Immunity *50*, 1132–1148. https://doi.org/10.1016/j.immuni.2019.04.011.
7. Vinuesa, C.G., Linterman, M.A., Yu, D., and MacLennan, I.C.M. (2016). Follicular Helper T Cells. Annu. Rev. Immunol. *34*, 335–368. https://doi.org/10.1146/annurev-immunol-041015-055605.
8. Lanzavecchia, A. (1985). Antigen-specific interaction between T and B cells. Nature *314*, 537–539. https://doi.org/10.1038/314537a0.
9. Rock, K.L., Benacerraf, B., and Abbas, A.K. (1984). Antigen presentation by hapten-specific B lymphocytes. I. Role of surface immunoglobulin receptors. J. Exp. Med. *160*, 1102–1113. https://doi.org/10.1084/jem.160.4.1102.
10. Guermonprez, P., England, P., Bedouelle, H., and Leclerc, C. (1998). The rate of dissociation between antibody and antigen determines the efficiency of antibody-mediated antigen presentation to T cells. J. Immunol. *161*, 4542–4548. https://doi.org/10.4049/jimmunol.161.9.4542.
11. Dal Porto, J.M., Haberman, A.M., Kelsoe, G., and Shlomchik, M.J. (2002). Very Low Affinity B Cells Form Germinal Centers, Become Memory B Cells, and Participate in Secondary Immune Responses When Higher Affinity Competition Is Reduced. J. Exp. Med. *195*, 1215–1221. https://doi.org/10.1084/jem.20011550.
12. Ray, R., Schiffner, T., Wang, X., Yan, Y., Rantalainen, K., Lee, C.D., Parikh, S., Reyes, R.A., Dale, G.A., Lin, Y.-C., et al. (2024). Affinity gaps among B cells in germinal centers drive the selection of MPER precursors. Nat. Immunol. *25*, 1083–1096. https://doi.org/10.1038/s41590-024-01844-7.
13. Shih, T.-A.Y., Meffre, E., Roederer, M., and Nussenzweig, M.C. (2002). Role of BCR affinity in T cell dependent antibody responses in vivo. Nat. Immunol. *3*, 570–575. https://doi.org/10.1038/ni803.
14. Shinnakasu, R., Inoue, T., Kometani, K., Moriyama, S., Adachi, Y., Nakayama, M., Takahashi, Y., Fukuyama, H., Okada, T., and Kurosaki, T. (2016). Regulated selection of germinal-center cells into the memory B cell compartment. Nat. Immunol. *17*, 861–869. https://doi.org/10.1038/ni.3460.
15. Viant, C., Weymar, G.H.J., Escolano, A., Chen, S., Hartweger, H., Cipolla, M., Gazumyan, A., and Nussenzweig, M.C. (2020). Antibody affinity shapes the choice between memory and germinal center B cell fates. Cell *183*, 1298–1311.e11. https://doi.org/10.1016/j.cell.2020.09.063.
16. Sutton, H.J., Gao, X., Kelly, H.G., Parker, B.J., Lofgren, M., Dacon, C., Chatterjee, D., Seder, R.A., Tan, J., Idris, A.H., et al. (2024). Lack of affinity signature for germinal center cells that have initiated plasma cell differentiation. Immunity *57*, 245–255.e5. https://doi.org/10.1016/j.immuni.2023.12.010.
17. Sprumont, A., Rodrigues, A., McGowan, S.J., Bannard, C., and Bannard, O. (2023). Germinal centers output clonally diverse plasma cell populations expressing high- and low-affinity antibodies. Cell *186*, 5486–5499.e13. https://doi.org/10.1016/j.cell.2023.10.022.
18. Foote, J., and Eisen, H.N. (1995). Kinetic and affinity limits on antibodies produced during immune responses. Proc. Natl. Acad. Sci. USA *92*, 1254–1256. https://doi.org/10.1073/pnas.92.5.1254.
19. Roost, H.P., Bachmann, M.F., Haag, A., Kalinke, U., Pliska, V., Hengartner, H., and Zinkernagel, R.M. (1995). Early high-affinity neutralizing anti-viral IgG responses without further overall improvements of affinity. Proc. Natl. Acad. Sci. USA *92*, 1257–1261. https://doi.org/10.1073/pnas.92.5.1257.
20. Finkelstein, M.S., and Uhr, J.W. (1964). SPECIFIC INHIBITION OF ANTIBODY FORMATION BY PASSIVELY ADMINISTERED 19S AND 7S ANTIBODY. Science *146*, 67–69. https://doi.org/10.1126/science.146.3640.67.
21. Henry, C., and Jerne, N.K. (1968). Competition of 19S and 7S antigen receptors in the regulation of the primary immune response. J. Exp. Med. *128*, 133–152. https://doi.org/10.1084/jem.128.1.133.
22. Heyman, B. (2000). Regulation of Antibody Responses via Antibodies, Complement, and Fc Receptors. Annu. Rev. Immunol. *18*, 709–737. https://doi.org/10.1146/annurev.immunol.18.1.709.
23. Smith, T. (1909). ACTIVE IMMUNITY PRODUCED BY SO CALLED BALANCED OR NEUTRAL MIXTURES OF DIPHTHERIA TOXIN AND ANTITOXIN. J. Exp. Med. *11*, 241–256. https://doi.org/10.1084/jem.11.2.241.
24. Heesters, B.A., Myers, R.C., and Carroll, M.C. (2014). Follicular dendritic cells: dynamic antigen libraries. Nat. Rev. Immunol. *14*, 495–504. https://doi.org/10.1038/nri3689.
25. Zhang, Y., Meyer-Hermann, M., George, L.A., Figge, M.T., Khan, M., Goodall, M., Young, S.P., Reynolds, A., Falciani, F., Waisman, A., et al. (2013). Germinal center B cells govern their own fate via antibody feedback. J. Exp. Med. *210*, 457–464. https://doi.org/10.1084/jem.20120150.

26. Pape, K.A., Taylor, J.J., Maul, R.W., Gearhart, P.J., and Jenkins, M.K. (2011). Different B cell populations mediate early and late memory during an endogenous immune response. Science *331*, 1203–1207. https://doi.org/10.1126/science.1201730.

27. Tas, J.M.J., Koo, J.-H., Lin, Y.-C., Xie, Z., Steichen, J.M., Jackson, A.M., Hauser, B.M., Wang, X., Cottrell, C.A., Torres, J.L., et al. (2022). Antibodies from primary humoral responses modulate the recruitment of naive B cells during secondary responses. Immunity *55*, 1856–1871.e6. https://doi.org/10.1016/j.immuni.2022.07.020.

28. Dvorscek, A.R., McKenzie, C.I., Stäheli, V.C., Ding, Z., White, J., Fabb, S.A., Lim, L., O'Donnell, K., Pitt, C., Christ, D., et al. (2024). Conversion of vaccines from low to high immunogenicity by antibodies with epitope complementarity. Immunity *57*, 2433–2452.e7. https://doi.org/10.1016/j.immuni.2024.08.017.

29. Schaefer-Babajew, D., Wang, Z., Muecksch, F., Cho, A., Loewe, M., Cipolla, M., Raspe, R., Johnson, B., Canis, M., DaSilva, J., et al. (2023). Antibody feedback regulates immune memory after SARS-CoV-2 mRNA vaccination. Nature *613*, 735–742. https://doi.org/10.1038/s41586-022-05609-w.

30. McNamara, H.A., Idris, A.H., Sutton, H.J., Vistein, R., Flynn, B.J., Cai, Y., Wiehe, K., Lyke, K.E., Chatterjee, D., Kc, N., et al. (2020). Antibody Feedback Limits the Expansion of B Cell Responses to Malaria Vaccination but Drives Diversification of the Humoral Response. Cell Host Microbe *28*, 572–585.e7. https://doi.org/10.1016/j.chom.2020.07.001.

31. Caniels, T.G., Prabhakaran, M., Ozorowski, G., MacPhee, K.J., Wu, W., van der Straten, K., Agrawal, S., Derking, R., Reiss, E.I.M.M., Millard, K., et al. (2025). Precise targeting of HIV broadly neutralizing antibody precursors in humans. Science *389*, eadv5572. https://doi.org/10.1126/science.adv5572.

32. Escolano, A., Steichen, J.M., Dosenovic, P., Kulp, D.W., Golijanin, J., Sok, D., Freund, N.T., Gitlin, A.D., Oliveira, T., Araki, T., et al. (2016). Sequential Immunization Elicits Broadly Neutralizing Anti-HIV-1 Antibodies in Ig Knockin Mice. Cell *166*, 1445–1458.e12. https://doi.org/10.1016/j.cell.2016.07.030.

33. Jardine, J.G., Julien, J.-P., Menis, S., Ota, T., Kalyuzhniy, O., McGuire, A., Sok, D., Huang, P.-S., MacPherson, S., Jones, M., et al. (2013). Rational HIV Immunogen Design to Target Specific Germline B Cell Receptors. Science *340*, 711–716. https://doi.org/10.1126/science.1234150.

34. Jardine, J.G., Ota, T., Sok, D., Pauthner, M., Kulp, D.W., Kalyuzhniy, O., Skog, P.D., Thinnes, T.C., Bhullar, D., Briney, B., et al. (2015). HIV-1 vaccines. Priming a broadly neutralizing antibody response to HIV-1 using a germline-targeting immunogen. Science *349*, 156–161. https://doi.org/10.1126/science.aac5894.

35. Leggat, D.J., Cohen, K.W., Willis, J.R., Fulp, W.J., deCamp, A.C., Kalyuzhniy, O., Cottrell, C.A., Menis, S., Finak, G., Ballweber-Fleming, L., et al. (2022). Vaccination induces HIV broadly neutralizing antibody precursors in humans. Science *378*, eadd6502. https://doi.org/10.1126/science.add6502.

36. Lin, X., Cottrell, C.A., Kalyuzhniy, O., Tingle, R., Kubitz, M., Lu, D., Yuan, M., Schief, W.R., and Wilson, I.A. (2025). Structural insights into VRC01-class bnAb precursors with diverse light chains elicited in the IAVI G001 human vaccine trial. Proc. Natl. Acad. Sci. USA *122*, e2510163122. https://doi.org/10.1073/pnas.2510163122.

37. McGuire, A.T., Hoot, S., Dreyer, A.M., Lippy, A., Stuart, A., Cohen, K.W., Jardine, J., Menis, S., Scheid, J.F., West, A.P., et al. (2013). Engineering HIV envelope protein to activate germline B cell receptors of broadly neutralizing anti-CD4 binding site antibodies. J. Exp. Med. *210*, 655–663. https://doi.org/10.1084/jem.20122824.

38. Sok, D., and Burton, D.R. (2018). Recent progress in broadly neutralizing antibodies to HIV. Nat. Immunol. *19*, 1179–1188. https://doi.org/10.1038/s41590-018-0235-7.

39. Steichen, J.M., Kulp, D.W., Tokatlian, T., Escolano, A., Dosenovic, P., Stanfield, R.L., McCoy, L.E., Ozorowski, G., Hu, X., Kalyuzhniy, O., et al. (2016). HIV Vaccine Design to Target Germline Precursors of Glycan-Dependent Broadly Neutralizing Antibodies. Immunity *45*, 483–496. https://doi.org/10.1016/j.immuni.2016.08.016.

40. Steichen, J.M., Lin, Y.C., Havenar-Daughton, C., Pecetta, S., Ozorowski, G., Willis, J.R., Toy, L., Sok, D., Liguori, A., Kratochvil, S., et al. (2019). A generalized HIV vaccine design strategy for priming of broadly neutralizing antibody responses. Science *366*, eaax4380. https://doi.org/10.1126/science.aax4380.

41. Willis, J.R., Prabhakaran, M., Muthui, M., Naidoo, A., Sincomb, T., Wu, W., Cottrell, C.A., Landais, E., deCamp, A.C., Keshavarzi, N.R., et al. (2025). Vaccination with mRNA-encoded nanoparticles drives early maturation of HIV bnAb precursors in humans. Science *389*, eadr8382. https://doi.org/10.1126/science.adr8382.

42. Xiao, X., Chen, W., Feng, Y., Zhu, Z., Prabakaran, P., Wang, Y., Zhang, M.-Y., Longo, N.S., and Dimitrov, D.S. (2009). Germline-like predecessors of broadly neutralizing antibodies lack measurable binding to HIV-1 envelope glycoproteins: Implications for evasion of immune responses and design of vaccine immunogens. Biochem. Biophys. Res. Commun. *390*, 404–409. https://doi.org/10.1016/j.bbrc.2009.09.029.

43. Chen, X., Zhou, T., Schmidt, S.D., Duan, H., Cheng, C., Chuang, G.-Y., Gu, Y., Louder, M.K., Lin, B.C., Shen, C.-H., et al. (2021). Vaccination induces maturation in a mouse model of diverse unmutated VRC01-class precursors to HIV-neutralizing antibodies with >50% breadth. Immunity *54*, 324–339.e8. https://doi.org/10.1016/j.immuni.2020.12.014.

44. Bolton, D.L., Pegu, A., Wang, K., McGinnis, K., Nason, M., Foulds, K., Letukas, V., Schmidt, S.D., Chen, X., Todd, J.P., et al. (2016). Human Immunodeficiency Virus Type 1 Monoclonal Antibodies Suppress Acute Simian-Human Immunodeficiency Virus Viremia and Limit Seeding of Cell-Associated Viral Reservoirs. J. Virol. *90*, 1321–1332. https://doi.org/10.1128/JVI.02454-15.

45. Diskin, R., Klein, F., Horwitz, J.A., Halper-Stromberg, A., Sather, D.N., Marcovecchio, P.M., Lee, T., West, A.P., Gao, H., Seaman, M.S., et al. (2013). Restricting HIV-1 pathways for escape using rationally designed anti–HIV-1 antibodies. J. Exp. Med. *210*, 1235–1249. https://doi.org/10.1084/jem.20130221.

46. Gaebler, C., Nogueira, L., Stoffel, E., Oliveira, T.Y., Breton, G., Millard, K.G., Turroja, M., Butler, A., Ramos, V., Seaman, M.S., et al. (2022). Prolonged viral suppression with anti-HIV-1 antibody therapy. Nature *606*, 368–374. https://doi.org/10.1038/s41586-022-04597-1.

47. Halper-Stromberg, A., Lu, C.-L., Klein, F., Horwitz, J.A., Bournazos, S., Nogueira, L., Eisenreich, T.R., Liu, C., Gazumyan, A., Schaefer, U., et al. (2014). Broadly Neutralizing Antibodies and Viral inducers decrease rebound from HIV-1 latent reservoirs in humanized mice. Cell *158*, 989–999. https://doi.org/10.1016/j.cell.2014.07.043.

48. Horwitz, J.A., Halper-Stromberg, A., Mouquet, H., Gitlin, A.D., Tretiakova, A., Eisenreich, T.R., Malbec, M., Gravemann, S., Billerbeck, E., Dorner, M., et al. (2013). HIV-1 suppression and durable control by combining single broadly neutralizing antibodies and antiretroviral drugs in humanized mice. Proc. Natl. Acad. Sci. USA *110*, 16538–16543. https://doi.org/10.1073/pnas.1315295110.

49. Klein, F., Halper-Stromberg, A., Horwitz, J.A., Gruell, H., Scheid, J.F., Bournazos, S., Mouquet, H., Spatz, L.A., Diskin, R., Abadir, A., et al. (2012). HIV therapy by a combination of broadly neutralizing antibodies in humanized mice. Nature *492*, 118–122. https://doi.org/10.1038/nature11604.

50. Nishimura, Y., Gautam, R., Chun, T.-W., Sadjadpour, R., Foulds, K.E., Shingai, M., Klein, F., Gazumyan, A., Golijanin, J., Donaldson, M., et al. (2017). EARLY ANTIBODY THERAPY CAN INDUCE LONG-LASTING IMMUNITY TO SHIV. Nature *543*, 559–563. https://doi.org/10.1038/nature21435.

51. Batista, F.D., and Neuberger, M.S. (2000). B cells extract and present immobilized antigen: implications for affinity discrimination. EMBO J. *19*, 513–520. https://doi.org/10.1093/emboj/19.4.513.

52. Huang, J., Kang, B.H., Ishida, E., Zhou, T., Griesman, T., Sheng, Z., Wu, F., Doria-Rose, N.A., Zhang, B., McKee, K., et al. (2016). Identification of

a CD4-Binding Site Antibody to HIV that Evolved Near-Pan Neutralization Breadth. Immunity *45*, 1108–1121. https://doi.org/10.1016/j.immuni.2016.10.027.

53. Jardine, J.G., Sok, D., Julien, J.-P., Briney, B., Sarkar, A., Liang, C.-H., Scherer, E.A., Henry Dunand, C.J.H., Adachi, Y., Diwanji, D., et al. (2016). Minimally Mutated HIV-1 Broadly Neutralizing Antibodies to Guide Reductionist Vaccine Design. PLoS Pathog. *12*, e1005815. https://doi.org/10.1371/journal.ppat.1005815.

54. Landais, E., Murrell, B., Briney, B., Murrell, S., Rantalainen, K., Berndsen, Z.T., Ramos, A., Wickramasinghe, L., Smith, M.L., Eren, K., et al. (2017). HIV Envelope Glycoform Heterogeneity and Localized Diversity Govern the Initiation and Maturation of a V2 Apex Broadly Neutralizing Antibody Lineage. Immunity *47*, 990–1003.e9. https://doi.org/10.1016/j.immuni.2017.11.002.

55. Lin, Y.-C., Pecetta, S., Steichen, J.M., Kratochvil, S., Melzi, E., Arnold, J., Dougan, S.K., Wu, L., Kirsch, K.H., Nair, U., et al. (2018). One-step CRISPR/Cas9 method for the rapid generation of human antibody heavy chain knock-in mice. EMBO J. *37*, e99243. https://doi.org/10.15252/embj.201899243.

56. Wang, X., Ray, R., Kratochvil, S., Melzi, E., Lin, Y.-C., Giguere, S., Xu, L., Warner, J., Cheon, D., Liguori, A., et al. (2021). Multiplexed CRISPR/CAS9-mediated engineering of pre-clinical mouse models bearing native human B cell receptors. EMBO J. *40*, e105926. https://doi.org/10.15252/embj.2020105926.

57. Parks, K.R., Moodie, Z., Allen, M.A., Yen, C., Furch, B.D., MacPhee, K.J., Ozorowski, G., Heptinstall, J., Hahn, W.O., Zheng, Z., et al. (2025). Vaccination with mRNA-encoded membrane-anchored HIV envelope trimers elicited tier 2 neutralizing antibodies in a phase 1 clinical trial. Sci. Transl. Med. *17*, eady6831. https://doi.org/10.1126/scitranslmed.ady6831.

58. Ramezani-Rad, P., Cottrell, C.A., Marina-Zárate, E., Liguori, A., Landais, E., Torres, J.L., Myers, A., Lee, J.H., Baboo, S., Flynn, C., et al. (2025). Vaccination with an mRNA-encoded membrane-bound HIV Envelope trimer induces neutralizing antibodies in animal models. Sci. Transl. Med. *17*, eadw0721. https://doi.org/10.1126/scitranslmed.adw0721.

59. Silva, M., Kato, Y., Melo, M.B., Phung, I., Freeman, B.L., Li, Z., Roh, K., Van Wijnbergen, J.W., Watkins, H., Enemuo, C.A., et al. (2021). A particulate saponin/TLR agonist vaccine adjuvant alters lymph flow and modulates adaptive immunity. Sci. Immunol. *6*, eabf1152. https://doi.org/10.1126/sciimmunol.abf1152.

60. De Silva, N.S., and Klein, U. (2015). Dynamics of B cells in germinal centres. Nat. Rev. Immunol. *15*, 137–148. https://doi.org/10.1038/nri3804.

61. Liu, S., Iorgulescu, J.B., Li, S., Borji, M., Barrera-Lopez, I.A., Shanmugam, V., Lyu, H., Morriss, J.W., Garcia, Z.N., Murray, E., et al. (2022). Spatial maps of T cell receptors and transcriptomes reveal distinct immune niches and interactions in the adaptive immune response. Immunity *55*, 1940–1952.e5. https://doi.org/10.1016/j.immuni.2022.09.002.

62. Stickels, R.R., Murray, E., Kumar, P., Li, J., Marshall, J.L., Di Bella, D.J., Arlotta, P., Macosko, E.Z., and Chen, F. (2021). Highly sensitive spatial transcriptomics at near-cellular resolution with Slide-seqV2. Nat. Biotechnol. *39*, 313–319. https://doi.org/10.1038/s41587-020-0739-1.

63. Cable, D.M., Murray, E., Zou, L.S., Goeva, A., Macosko, E.Z., Chen, F., and Irizarry, R.A. (2022). Robust decomposition of cell type mixtures in spatial transcriptomics. Nat. Biotechnol. *40*, 517–526. https://doi.org/10.1038/s41587-021-00830-w.

64. Massoni-Badosa, R., Aguilar-Fernández, S., Nieto, J.C., Soler-Vila, P., Elosua-Bayes, M., Marchese, D., Kulis, M., Vilas-Zornoza, A., Bühler, M.M., Rashmi, S., et al. (2024). An atlas of cells in the human tonsil. Immunity *57*, 379–399.e18. https://doi.org/10.1016/j.immuni.2024.01.006.

65. Economopoulos, V., Noad, J.C., Krishnamoorthy, S., Rutt, B.K., and Foster, P.J. (2011). Comparing the MRI Appearance of the Lymph Nodes and Spleen in Wild-Type and Immuno-Deficient Mouse Strains. PLoS One *6*, e27508. https://doi.org/10.1371/journal.pone.0027508.

66. Najibi, A.J., Lane, R.S., Sobral, M.C., Bovone, G., Kang, S., Freedman, B.R., Gutierrez Estupinan, J., Elosegui-Artola, A., Tringides, C.M., Dellacherie, M.O., et al. (2024). Durable lymph-node expansion is associated with the efficacy of therapeutic vaccination. Nat. Biomed. Eng. *8*, 1226–1242. https://doi.org/10.1038/s41551-024-01209-3.

67. Assen, F.P., Abe, J., Hons, M., Hauschild, R., Shamipour, S., Kaufmann, W.A., Costanzo, T., Krens, G., Brown, M., Ludewig, B., et al. (2022). Multitier mechanics control stromal adaptations in the swelling lymph node. Nat. Immunol. *23*, 1246–1255. https://doi.org/10.1038/s41590-022-01257-4.

68. Huh, Y.-M., Kim, S., Suh, J.-S., Song, H.T., Song, K., and Shin, K.-H. (2005). The Role of Popliteal Lymph Nodes in Differentiating Rheumatoid Arthritis from Osteoarthritis by Using CE 3D-FSPGR MR Imaging: Relationship of the Inflamed Synovial Volume. Korean J. Radiol. *6*, 117–124. https://doi.org/10.3348/kjr.2005.6.2.117.

69. Kammüller, M.E., Thomas, C., De Bakker, J.M., Bloksma, N., and Seinen, W. (1989). The popliteal lymph node assay in mice to screen for the immune disregulating potential of chemicals — A preliminary study. Int. J. Immunopharmacol. *11*, 293–300. https://doi.org/10.1016/0192-0561(89)90167-7.

70. Thomas, C., Lippe, W., Seinen, W., and Bloksma, N. (1991). Popliteal lymph node enlargement and antibody production in the mouse induced by drugs affecting monoamine levels in the brain. Int. J. Immunopharmacol. *13*, 621–629. https://doi.org/10.1016/0192-0561(91)90174-6.

71. Victora, G.D., and Nussenzweig, M.C. (2022). Germinal Centers. Annu. Rev. Immunol. *40*, 413–442. https://doi.org/10.1146/annurev-immunol-120419-022408.

72. Chan, T.D., and Brink, R. (2012). Affinity-based selection and the germinal center response. Immunol. Rev. *247*, 11–23. https://doi.org/10.1111/j.1600-065X.2012.01118.x.

73. Kwak, K., Quizon, N., Sohn, H., Saniee, A., Manzella-Lapeira, J., Holla, P., Brzostowski, J., Lu, J., Xie, H., Xu, C., et al. (2018). Intrinsic properties of human germinal center B cells set antigen affinity thresholds. Sci. Immunol. *3*, eaau6598. https://doi.org/10.1126/sciimmunol.aau6598.

74. Schwickert, T.A., Victora, G.D., Fooksman, D.R., Kamphorst, A.O., Mugnier, M.R., Gitlin, A.D., Dustin, M.L., and Nussenzweig, M.C. (2011). A dynamic T cell–limited checkpoint regulates affinity-dependent B cell entry into the germinal center. J. Exp. Med. *208*, 1243–1252. https://doi.org/10.1084/jem.20102477.

75. Kuraoka, M., Schmidt, A.G., Nojima, T., Feng, F., Watanabe, A., Kitamura, D., Harrison, S.C., Kepler, T.B., and Kelsoe, G. (2016). Complex Antigens Drive Permissive Clonal Selection in Germinal Centers. Immunity *44*, 542–552. https://doi.org/10.1016/j.immuni.2016.02.010.

76. Schiepers, A., Van't Wout, M.F.L., Hobbs, A., Mesin, L., and Victora, G.D. (2024). Opposing effects of pre-existing antibody and memory T cell help on the dynamics of recall germinal centers. Immunity *57* (7), 1618–1628.e4. https://doi.org/10.1016/j.immuni.2024.05.009.

77. Meyer-Hermann, M. (2019). Injection of Antibodies against Immunodominant Epitopes Tunes Germinal Centers to Generate Broadly Neutralizing Antibodies. Cell Rep. *29*, 1066–1073.e5. https://doi.org/10.1016/j.celrep.2019.09.058.

78. Inoue, T., Shinnakasu, R., Kawai, C., Yamamoto, H., Sakakibara, S., Ono, C., Itoh, Y., Terooatea, T., Yamashita, K., Okamoto, T., et al. (2022). Antibody feedback contributes to facilitating the development of Omicron-reactive memory B cells in SARS-CoV-2 mRNA vaccinees. J. Exp. Med. *220*, e20221786. https://doi.org/10.1084/jem.20221786.

79. Li, R., Bao, K., Liu, C., Ma, X., Hua, Z., Zhu, P., and Hou, B. (2025). Competition propels, rather than limits, the success of low-affinity B cells in the germinal center response. Cell Rep. *44*, 115334. https://doi.org/10.1016/j.celrep.2025.115334.

80. Madden, P.J., Marina-Zárate, E., Rodrigues, K.A., Steichen, J.M., Shil, M., Ni, K., Michaels, K.K., Maiorino, L., Upadhyay, A.A., Saha, S., et al. (2025). Diverse priming outcomes under conditions of very rare precursor

B cells. Immunity *58*, 997–1014.e11. https://doi.org/10.1016/j.immuni.2025.03.003.

81. Ise, W., Fujii, K., Shiroguchi, K., Ito, A., Kometani, K., Takeda, K., Kawakami, E., Yamashita, K., Suzuki, K., Okada, T., et al. (2018). T Follicular Helper Cell-Germinal Center B Cell Interaction Strength Regulates Entry into Plasma Cell or Recycling Germinal Center Cell Fate. Immunity *48*, 702–715.e4. https://doi.org/10.1016/j.immuni.2018.03.027.

82. Kräutler, N.J., Suan, D., Butt, D., Bourne, K., Hermes, J.R., Chan, T.D., Sundling, C., Kaplan, W., Schofield, P., Jackson, J., et al. (2017). Differentiation of germinal center B cells into plasma cells is initiated by high-affinity antigen and completed by Tfh cells. J. Exp. Med. *214*, 1259–1267. https://doi.org/10.1084/jem.20161533.

83. Nutt, S.L., Hodgkin, P.D., Tarlinton, D.M., and Corcoran, L.M. (2015). The generation of antibody-secreting plasma cells. Nat. Rev. Immunol. *15*, 160–171. https://doi.org/10.1038/nri3795.

84. Angelin-Duclos, C., Cattoretti, G., Lin, K.I., and Calame, K. (2000). Commitment of B Lymphocytes to a Plasma Cell Fate Is Associated with Blimp-1 Expression In Vivo1. J. Immunol. *165*, 5462–5471. https://doi.org/10.4049/jimmunol.165.10.5462.

85. Zhang, Y., Tech, L., George, L.A., Acs, A., Durrett, R.E., Hess, H., Walker, L.S.K., Tarlinton, D.M., Fletcher, A.L., Hauser, A.E., et al. (2018). Plasma cell output from germinal centers is regulated by signals from Tfh and stromal cells. J. Exp. Med. *215*, 1227–1243. https://doi.org/10.1084/jem.20160832.

86. ElTanbouly, M.A., Ramos, V., MacLean, A.J., Chen, S.T., Loewe, M., Steinbach, S., Ben Tanfous, T., Johnson, B., Cipolla, M., Gazumyan, A., et al. (2023). Role of affinity in plasma cell development in the germinal center light zone. J. Exp. Med. *221*, e20231838. https://doi.org/10.1084/jem.20231838.

87. Aung, A., Cui, A., Maiorino, L., Amini, A.P., Gregory, J.R., Bukenya, M., Zhang, Y., Lee, H., Cottrell, C.A., Morgan, D.M., et al. (2023). Low protease activity in B cell follicles promotes retention of intact antigens after immunization. Science *379*, eabn8934. https://doi.org/10.1126/science.abn8934.

88. MacLean, A.J., Deimel, L.P., Zhou, P., ElTanbouly, M.A., Merkenschlager, J., Ramos, V., Santos, G.S., Hägglöf, T., Mayer, C.T., Hernandez, B., et al. (2025). Affinity maturation of antibody responses is mediated by differential plasma cell proliferation. Science *387*, 413–420. https://doi.org/10.1126/science.adr6896.

89. Abbott, R.K., and Crotty, S. (2020). Factors in B cell competition and immunodominance. Immunol. Rev. *296*, 120–131. https://doi.org/10.1111/imr.12861.

90. Cottrell, C.A., Hu, X., Lee, J.H., Skog, P., Luo, S., Flynn, C.T., McKenney, K.R., Hurtado, J., Kalyuzhniy, O., Liguori, A., et al. (2024). Heterologous prime-boost vaccination drives early maturation of HIV broadly neutralizing antibody precursors in humanized mice. Sci. Transl. Med. *16*, eadn0223. https://doi.org/10.1126/scitranslmed.adn0223.

91. Wang, X., Cottrell, C.A., Hu, X., Ray, R., Bottermann, M., Villavicencio, P.M., Yan, Y., Xie, Z., Warner, J.E., Ellis-Pugh, J.R., et al. (2024). mRNA-LNP prime boost evolves precursors toward VRC01-like broadly neutralizing antibodies in preclinical humanized mouse models. Sci. Immunol. *9*, eadn0622. https://doi.org/10.1126/sciimmunol.adn0622.

92. Xie, Z., Lin, Y.-C., Steichen, J.M., Ozorowski, G., Kratochvil, S., Ray, R., Torres, J.L., Liguori, A., Kalyuzhniy, O., Wang, X., et al. (2024). mRNA-LNP HIV-1 trimer boosters elicit precursors to broad neutralizing antibodies. Science *384*, eadk0582. https://doi.org/10.1126/science.adk0582.

93. Xie, Z., Wang, X., Yan, Y., Steichen, J.M., Ma, K.M., Cottrell, C.A., Melzi, E., Bottermann, M., Villavicencio, P.M., Rantalainen, K., et al. (2025). Simultaneous priming of HIV broadly neutralizing antibody precursors to multiple epitopes by germline-targeting mRNA-LNP immunogens in mouse models. Sci. Immunol. *10*, eadu7961. https://doi.org/10.1126/sciimmunol.adu7961.

94. Sutton, H.J., Ma, K.M., Steichen, J.M., Schiffner, T., Altheide, T.K., Liguori, A., Lu, D., Kubitz, M., Georgeson, E., Phelps, N., et al. (2025). Simultaneous induction of multiple classes of broadly neutralizing antibody precursors by combination germline-targeting immunization in nonhuman primates. Sci. Immunol. *10*, eadu8878. https://doi.org/10.1126/sciimmunol.adu8878.

95. Lanoue, A., Batista, F.D., Stewart, M., and Neuberger, M.S. (2002). Interaction of CD22 with alpha2,6-linked sialoglycoconjugates: innate recognition of self to dampen B cell autoreactivity? Eur. J. Immunol. *32*, 348–355. https://doi.org/10.1002/1521-4141(200202)32:2<348::AID-IMMU348>3.0.CO;2-5.

96. Melzi, E., Willis, J.R., Ma, K.M., Lin, Y.-C., Kratochvil, S., Berndsen, Z.T., Landais, E.A., Kalyuzhniy, O., Nair, U., Warner, J., et al. (2022). Membrane-bound mRNA immunogens lower the threshold to activate HIV Env V2 apex-directed broadly neutralizing B cell precursors in humanized mice. Immunity *55*, 2168–2186.e6. https://doi.org/10.1016/j.immuni.2022.09.003.

97. Kallewaard N.L., Corti D., Collins P.J., Neu U., McAuliffe J.M., Benjamin E., Wachter-Rosati L., Palmer-Hill F.J., Yuan A.Q., Walker P.A., et al. Structure and Function Analysis of an Antibody Recognizing All Influenza A Subtypes. Cell. 2016 Jul 28;166(3):596-608. doi: 10.1016/j.cell.2016.05.073.

98. Moore, J.P., Trkola, A., Korber, B., Boots, L.J., Kessler, J.A., II, McCutchan, F.E., Mascola, J., Ho, D.D., Robinson, J., and Conley, A.J. (1995 Jan). A human monoclonal antibody to a complex epitope in the V3 region of gp120 of human immunodeficiency virus type 1 has broad reactivity within and outside clade B. J Virol *69* (1), 122–130. https://doi.org/10.1128/JVI.69.1.122-130.1995.

99. Marasco, W.A., Bagley, J., Zani, C., Posner, M., Cavacini, L., Haseltine, W.A., and Sodroski, J. (1992 Oct). Characterization of the cDNA of a broadly reactive neutralizing human anti-gp120 monoclonal antibody. J Clin Invest *90* (4), 1467–1478. https://doi.org/10.1172/JCI116014.

100. Pantophlet, R., Saphire, E.O., Poignard, P., Parren, P.W., Wilson, I.A., and Burton, D.R. (2003 Jan). Fine mapping of the interaction of neutralizing and nonneutralizing monoclonal antibodies with the CD4 binding site of human immunodeficiency virus type 1 gp120. J Virol *77* (1), 642–658. https://doi.org/10.1128/jvi.77.1.642-658.2003.

101. Walker L.M., Huber M., Doores K.J., Falkowska E., Pejchal R., Julien J.P., Wang S.K., Ramos A., Chan-Hui P.Y., Moyle M., et al. Protocol G Principal Investigators; Koff WC, Wilson IA, Burton DR, Poignard P. Broad neutralization coverage of HIV by multiple highly potent antibodies. Nature. 2011 Sep 22;477(7365):466-70. doi: 10.1038/nature10373.

102. Falkowska E., Le K.M., Ramos A., Doores K.J., Lee J.H., Blattner C., Ramirez A., Derking R., van Gils M.J., Liang C.H., et al. Broadly neutralizing HIV antibodies define a glycan-dependent epitope on the prefusion conformation of gp41 on cleaved envelope trimers. Immunity. 2014 May 15;40(5):657-68. doi: 10.1016/j.immuni.2014.04.009.

103. Scheid J.F., Mouquet H., Ueberheide B., Diskin R., Klein F., Oliveira T.Y., Pietzsch J., Fenyo D., Abadir A., Velinzon K., et al. Sequence and structural convergence of broad and potent HIV antibodies that mimic CD4 binding. Science. 2011 Sep 16;333(6049):1633-7. doi: 10.1126/science.1207227.

104. Schindelin J., Arganda-Carreras I., Frise E., Kaynig V., Longair M., Pietzsch T., Preibisch S., Rueden C., Saalfeld S., Schmid B., et al. Fiji: an open-source platform for biological-image analysis. Nat Methods. 2012 Jun 28;9(7):676-82. doi: 10.1038/nmeth.2019.

105. Wolf, F.A., Angerer, P., and Theis, F.J. (2018). SCANPY: large-scale single-cell gene expression data analysis. Genome Biol *19* (1), 15. https://doi.org/10.1186/s13059-017-1382-0.

106. Goddard, T.D., Huang, C.C., Meng, E.C., Pettersen, E.F., Couch, G.S., Morris, J.H., and Ferrin, T.E. (2018 Jan). UCSF ChimeraX: Meeting

modern challenges in visualization and analysis. Protein Sci *27* (1), 14–25. https://doi.org/10.1002/pro.3235.

107. Li, M., Salazar-Gonzalez, J.F., Derdeyn, C.A., Morris, L., Williamson, C., Robinson, J.E., Decker, J.M., Li, Y., Salazar, M.G., Polonis, V.R., et al. (2006). Genetic and Neutralization Properties of Subtype C Human Immunodeficiency Virus Type 1 Molecular env Clones from Acute and Early Heterosexually Acquired Infections in Southern Africa. J. Virol. *80*, 11776–11790. https://doi.org/10.1128/jvi.01730-06.

108. Binley, J.M., Sanders, R.W., Clas, B., Schuelke, N., Master, A., Guo, Y., Kajumo, F., Anselma, D.J., Maddon, P.J., Olson, W.C., et al. (2000). A recombinant human immunodeficiency virus type 1 envelope glycoprotein complex stabilized by an intermolecular disulfide bond between the gp120 and gp41 subunits is an antigenic mimic of the trimeric virion-associated structure. J. Virol. *74*, 627–643. https://doi.org/10.1128/jvi.74.2.627-643.2000.

109. Sanders, R.W., Vesanen, M., Schuelke, N., Master, A., Schiffner, L., Kalyanaraman, R., Paluch, M., Berkhout, B., Maddon, P.J., Olson, W.C., et al. (2002). Stabilization of the soluble, cleaved, trimeric form of the envelope glycoprotein complex of human immunodeficiency virus type 1. J. Virol. *76*, 8875–8889. https://doi.org/10.1128/jvi.76.17.8875-8889.2002.

110. Sanders, R.W., Derking, R., Cupo, A., Julien, J.-P., Yasmeen, A., de Val, N., Kim, H.J., Blattner, C., de la Peña, A.T., Korzun, J., et al. (2013). A next-generation cleaved, soluble HIV-1 Env trimer, BG505 SOSIP.664 gp140, expresses multiple epitopes for broadly neutralizing but not non-neutralizing antibodies. PLoS Pathog. *9*, e1003618. https://doi.org/10.1371/journal.ppat.1003618.

111. Klasse, P.J., Depetris, R.S., Pejchal, R., Julien, J.-P., Khayat, R., Lee, J.H., Marozsan, A.J., Cupo, A., Cocco, N., Korzun, J., et al. (2013). Influences on Trimerization and Aggregation of Soluble, Cleaved HIV-1 SOSIP Envelope Glycoprotein. J. Virol. *87*, 9873–9885. https://doi.org/10.1128/JVI.01226-13.

112. Sok, D., Briney, B., Jardine, J.G., Kulp, D.W., Menis, S., Pauthner, M., Wood, A., Lee, E.-C., Le, K.M., Jones, M., et al. (2016). Priming HIV-1 broadly neutralizing antibody precursors in human Ig loci transgenic mice. Science *353*, 1557–1560. https://doi.org/10.1126/science.aah3945.

113. Allen, J.D., Ivory, D.P., Song, S.G., He, W.T., Capozzola, T., Yong, P., Burton, D.R., Andrabi, R., and Crispin, M. (2023). The diversity of the glycan shield of sarbecoviruses related to SARS-CoV-2. Cell Rep. *42*, 112307. https://doi.org/10.1016/j.celrep.2023.112307.

114. Rodriques, S.G., Stickels, R.R., Goeva, A., Martin, C.A., Murray, E., Vanderburg, C.R., Welch, J., Chen, L.M., Chen, F., and Macosko, E.Z. (2019). Slide-seq: A scalable technology for measuring genome-wide expression at high spatial resolution. Science *363*, 1463–1467. https://doi.org/10.1126/science.aaw1219.

115. Ester, M., Kriegel, H.-P., Sander, J., and Xu, X. (1996). A density-based algorithm for discovering clusters in large spatial databases with noise. In Proceedings of the Second International Conference on Knowledge Discovery and Data Mining KDD'96 (A.A.A.I. Press), pp. 226–231.

116. Dyer, S.C., Austine-Orimoloye, O., Azov, A.G., Barba, M., Barnes, I., Barrera-Enriquez, V.P., Becker, A., Bennett, R., Beracochea, M., Berry, A., et al. (2025). Ensembl 2025. Nucleic Acids Res. *53*, D948–D957. https://doi.org/10.1093/nar/gkae1071.

## STAR★METHODS

### KEY RESOURCES TABLE

| REAGENT or RESOURCE | SOURCE | IDENTIFIER |
|---|---|---|
| Antibodies | | |
| PE/Cy7 anti-mouse IgD Antibody | Biolegend | Cat#: 405720; RRID: AB_2738061 |
| APC/Cy7 anti-mouse/human CD45R/ B220 Antibody | Biolegend | Cat#: 103224; RRID: AB_313007 |
| BV711 Rat Anti-Mouse Ig, λ1, λ2 & λ3 Light Chain | BD Biosciences | Cat#: 744527; RRID: AB_2742301 |
| BUV395 Rat Anti-Mouse Ig, κ light chain | BD Biosciences | Cat#: 742839; RRID: AB_2741090 |
| BV421 Rat Anti-Mouse IgM | BD Biosciences | Cat#: 743323; RRID: AB_2741424 |
| PE anti-mouse CD45.2 Antibody | Biolegend | Cat#: 109808; RRID: AB_313445 |
| BV786 Rat Anti-Mouse IgD | BD Biosciences | Cat#: 563618; RRID: AB_2738322 |
| BV421 Rat Anti-Mouse IgG1 | BD Biosciences | Cat#: 562580; RRID: AB_2737664 |
| BUV395 Rat Anti-Mouse IgM | BD Biosciences | Cat#: 743329; RRID: AB_2741430 |
| Alexa Fluor® 594 anti-mouse IgD Antibody | Biolegend | Cat#: 405740; RRID: AB_2565572 |
| BV786 Rat Anti-Mouse IgM | BD Biosciences | Cat#: 564028; RRID: AB_2738553 |
| BV785 anti-mouse CD138 (Syndecan-1) Antibody | Biolegend | Cat#: 142534; RRID: AB_2814047 |
| anti-mouse CD38, BV510 | BD Biosciences | Cat#: 740129; RRID: AB_2739886 |
| PE anti-mouse CD138 (Syndecan-1) Antibody | Biolegend | Cat#: 142503; RRID: AB_10915989 |
| Alexa Fluor® 700 anti-mouse IgD Antibody | Biolegend | Cat#: 405729; RRID: AB_2563340 |
| anti-mouse CD38, BV510 | BD Biosciences | Cat#: 740129; RRID: AB_2739886 |
| PE Hamster Anti-Mouse CD95 | BD Biosciences | Cat#: 561985; RRID: AB_10895586 |
| PE/Cyanine7 anti-mouse CD138 (Syndecan-1) Antibody | Biolegend | Cat#: 142513; RRID: AB_2562197 |
| BUV395 Rat Anti-Mouse IgG2b | BD Biosciences | Cat#: 743180; RRID: AB_2741331 |
| Alexa Fluor® 594 AffiniPure® Goat Anti-Mouse IgG2c | Jackson ImmunoResearch | Cat#: 115-587-188; RRID: AB_2632542 |
| CD4 Monoclonal Antibody (GK1.5), APC-eFluor 780 | Thermo Fisher Scientific | Cat#: 47-0041-82; RRID: AB_11218896 |
| CD8a Monoclonal Antibody (53–6.7), APC-eFluor 780 | Thermo Fisher Scientific | Cat#: 47-0081-82; RRID: AB_1272185 |
| F4/80 Monoclonal Antibody (BM8), APC-eFluor 780 | Thermo Fisher Scientific | Cat#: 47-4801-82; RRID: AB_2735036 |
| Ly-6G Monoclonal Antibody (1A8-Ly6g), APC-eFluor 780 | Thermo Fisher Scientific | Cat#: 47-9668-82; RRID: AB_2802291 |
| Alexa Fluor® 700 anti-mouse CD4 Antibody | Biolegend | Cat#: 100429; RRID: AB_493698 |
| CD8a Monoclonal Antibody (53–6.7), Alexa Fluor™ 700 | Thermo Fisher Scientific | Cat#: 56-0081-82; RRID: AB_494005 |
| Alexa Fluor® 700 anti-mouse F4/80 Antibody | Biolegend | Cat#: 123129; RRID: AB_2277848 |
| Alexa Fluor® 700 anti-mouse Ly-6G Antibody | Biolegend | Cat#: 127621; RRID: AB_10640452 |
| APC/Cyanine7 anti-mouse CD23 Antibody | Biolegend | Cat#: 101629; RRID: AB_2571986 |
| BUV395 Rat Anti-Mouse CD21/CD35 | BD Biosciences | Cat#: 740249; RRID: AB_2739995 |
| PE/Cyanine7 anti-mouse CD24 Antibody | Biolegend | Cat#: 101821; RRID: AB_756047 |
| PE anti-mouse CD43 Antibody | Biolegend | Cat#: 143205; RRID: AB_11142681 |
| BV786 rat anti-mouse IgM Antibody | BD Biosciences | Cat#: 743328; RRID: AB_2741429 |
| BV421 anti-mouse IgD Antibody | Biolegend | Cat#: 405725; RRID: AB_2562743 |
| PerCP/Cyanine5.5 anti-mouse CD93 (AA4.1, early B lineage) Antibody | Biolegend | Cat#: 136511; RRID: AB_10645333 |
| BUV395 Rat Anti-Mouse CD45R/B220 | BD Biosciences | Cat#: 563793; RRID: AB_2738427 |
| BUV805 Rat Anti-CD11b | BD Biosciences | Cat#: 568345; RRID: AB_2941960 |

(*Continued on next page*)

*Continued*

| REAGENT or RESOURCE | SOURCE | IDENTIFIER |
|---|---|---|
| BV605 Rat Anti-Mouse CD5 | BD Biosciences | Cat#: 563194; RRID: AB_2738061 |
| BV650 Rat Anti-Mouse CD23 | BD Biosciences | Cat#: 740456; RRID: AB_2740183 |
| PE anti-mouse CD23 Antibody | Biolegend | Cat#: 101608; RRID: AB_312833 |
| PE/Cyanine7 anti-mouse IgM Antibody | Biolegend | Cat#: 406514; RRID: AB_10642031 |
| PE/Cyanine7 anti-mouse CD19 Antibody | Biolegend | Cat#: 152418; RRID: AB_2927870 |
| PerCP/Cyanine5.5 anti-mouse/human CD45R/B220 Antibody | Biolegend | Cat#: 103236; RRID: AB_893354 |
| Alexa Fluor® 488 anti-mouse CD45.2 Antibody | Biolegend | Cat#: 109816; RRID: AB_492868 |
| Alexa Fluor® 594 anti-mouse/human CD45R/B220 Antibody | Biolegend | Cat#: 103254; RRID: AB_2563229 |
| Alexa Fluor® 647 anti-IRF4 Antibody | Biolegend | Cat#: 646408; RRID: AB_2564048 |
| MEDI8852 Ab | Kallewaard et al.[97] | N/A |
| 19b Ab | Moore et al.[98] | N/A |
| F105 Ab | Marasco et al.[99] | N/A |
| B6 Ab | Pantophlet et al.[100] | N/A |
| PGT145 Ab | Walker et al.[101] | N/A |
| PGT151 Ab | Falkowska et al.[102] | N/A |
| PGT121 Ab | Walker et al.[101] | RRID: AB_2491041 |
| N6 Ab | Huang et al.[52] | N/A |
| 12A21 Ab | Scheid et al.[103] | N/A |
| Min12A21 Ab | Jardine et al.[53] | N/A |
| N6-I2 Ab | Huang et al.[52] | N/A |
| N6-I3 Ab | Huang et al.[52] | N/A |
| PCT64-18D Ab | Landais et al.[54] | N/A |
| minBG18.6-1 Ab | This paper. | N/A |
| minBG18.6-2 Ab | This paper. | N/A |
| minBG18.6-3 Ab | This paper. | N/A |
| minBG18.6-4 Ab | This paper. | N/A |
| minBG18.11-1 Ab | This paper. | N/A |
| minBG18.11-2 Ab | This paper. | N/A |
| minBG18.11-3 Ab | This paper. | N/A |
| minBG18.11-4 Ab | This paper. | N/A |
| N6-I3-D7-1 Ab | This paper. | N/A |
| N6-I3-D7-2 Ab | This paper. | N/A |
| N6-I3-D7-3 Ab | This paper. | N/A |
| N6-I3-D7-4 Ab | This paper. | N/A |
| N6-I3-D7-5 Ab | This paper. | N/A |
| N6-I3-D7-6 Ab | This paper. | N/A |
| N6-I3-D7-7 Ab | This paper. | N/A |
| N6-I3-D7-8 Ab | This paper. | N/A |
| N6-I3-D7-9 Ab | This paper. | N/A |
| Min12A21-D7-1 Ab | This paper. | N/A |
| Min12A21-D7-2 Ab | This paper. | N/A |
| Min12A21-D7-3 Ab | This paper. | N/A |
| Min12A21-D7-4 Ab | This paper. | N/A |
| Min12A21-D7-5 Ab | This paper. | N/A |
| Min12A21-D7-6 Ab | This paper. | N/A |
| Min12A21-D7-7 Ab | This paper. | N/A |
| Min12A21-D7-8 Ab | This paper. | N/A |

(*Continued on next page*)

*Continued*

| REAGENT or RESOURCE | SOURCE | IDENTIFIER |
|---|---|---|
| Min12A21-D7-9 Ab | This paper. | N/A |
| **Bacterial and virus strains** | | |
| DH5α Competent Cells | Thermo Fisher Scientific | Cat # GACC-96 |
| **Chemicals, Peptides, and Recombinant Proteins** | | |
| Saponin/MPLA nanoparticles (SMNP) | Silva et al.[59] | N/A |
| Invitrogen™ Molecular Probes™ DAPI (4',6-Diamidino-2-Phenylindole, Dihydrochloride) | Thermo Fisher Scientific | Cat#: D1306 |
| Alexa Fluor 488 Streptavidin | Biolegend | Cat#: 405235 |
| Alexa Fluor 647 Streptavidin | Biolegend | Cat#: 405237 |
| Alexa Fluor 594 Streptavidin | Biolegend | Cat#: 405240 |
| SuperScript™ III Reverse Transcriptase | Thermo Fisher | Cat#: 18080085 |
| HotStarTaq DNA Polymerase | Qiagen | Cat#: 203205 |
| cOmplete™, EDTA-free Protease Inhibitor Cocktail | MilliporeSigma | Cat#: 12352204 |
| RNasin® Ribonuclease Inhibitors (Recombinant) | Promega | Cat#: N2515 |
| CountBright™ Absolute Counting Beads, for flow cytometry | Thermo Fisher Scientific | Cat#: C36950 |
| SIGMAFAST™ p-Nitrophenyl phosphate Tablets | MilliporeSigma | Cat#: N2770-50SET |
| NP40 | MilliporeSigma | Cat#: 492016-100ML |
| UltraComp eBeads™ Compensation Beads | Thermo Fisher Scientific | Cat#: 01-2222-42 |
| Recombinant Mouse IL-4 Protein | R and D systems | Cat#: 404-ML-025 |
| Recombinant Mouse IL-5 Protein | R and D systems | Cat#: 405-ML-025 |
| Recombinant Mouse CD40 Ligand/TNFSF5 (HA-tag) Protein | R and D systems | Cat#: 8230-CL-050 |
| RPMI 1640 Medium | Thermo Fisher Scientific | Cat#: 11875119 |
| Fetal Bovine Serum | MilliporeSigma | Cat#: F4135-500ML |
| HEPES | Thermo Fisher Scientific | Cat#: 15630080 |
| GlutaMAX™ Supplement | Thermo Fisher Scientific | Cat#: 35050079 |
| MEM Non-Essential Amino Acids Solution | Thermo Fisher Scientific | Cat#: 11140076 |
| Penicillin-Streptomycin | Thermo Fisher Scientific | Cat#: 15140122 |
| β-mercaptoethanol | MilliporeSigma | Cat#: M6250-100ML |
| DU172-17 MD39.2 SOSIP | This paper. | N/A |
| DU172-17 MD39 SOSIP CD4bs-KO (His-Avi-tagged) | This paper. | N/A |
| DU172-17 MD39 SOSIP (His-Avi-tagged) | This paper. | N/A |
| DU172-17 MD39 SOSIP (His-tagged) | This paper. | N/A |
| BG505 MD39.3 SOSIP | Ramezani-Rad et al.[58] | N/A |
| BG505 MD39.3 gp151 mRNA | Ramezani-Rad et al.[58] | N/A |
| BG505 MD39.3 SOSIP (His-Avi-tagged) | Ramezani-Rad et al.[58] | N/A |
| BG505 MD39.3 SOSIP CD4bs-KO (His-Avi-tagged) | Ramezani-Rad et al.[58] | N/A |
| BG505 MD39.3 SOSIP V2-KO (His-Avi-tagged) | This paper. | N/A |
| BG505 MD39.3 SOSIP V3-KO (His-Avi-tagged) | This paper. | N/A |
| BG505 MD39.3 SOSIP (His-tagged) | Ramezani-Rad et al.[58] | N/A |
| BG505 MD39.3 SOSIP CD4bs-KO (His-tagged) | Ramezani-Rad et al.[58] | N/A |
| Saponin/MPLA nanoparticles (SMNP) | Silva et al.[59] | N/A |
| **Critical commercial assays** | | |
| LIVE/DEAD™ Fixable Blue Dead Cell Stain Kit, for UV excitation | Thermo Fisher Scientific | Cat#: L34962 |
| LIVE/DEAD™ Fixable Violet Dead Cell Stain Kit, for 405 nm excitation | Thermo Fisher Scientific | Cat#: L34964 |

(*Continued on next page*)

*Continued*

| REAGENT or RESOURCE | SOURCE | IDENTIFIER |
|---|---|---|
| CellTrace™ CFSE Cell Proliferation Kit, for flow cytometry | Thermo Fisher Scientific | Cat#: C34554 |
| Pan B Cell Isolation Kit II, mouse | Miltenyi Biotec | Cat#: 130-104-443 |
| Chromium Next GEM Single Cell 5′ Kit v2 | 10x Genomics | PN-1000263 |
| Library Construction Kit | 10x Genomics | PN-1000190 |
| Chromium Single Cell Mouse BCR Amplification Kit | 10x Genomics | PN-1000255 |
| Chromium Next GEM Chip K Single Cell Kit | 10x Genomics | PN-1000286 |
| Dual Index Kit TT Set A | 10x Genomics | PN-1000215 |
| Dual Index Kit TN Set A | 10x Genomics | PN-1000250 |
| **Deposited data** | | |
| Raw and analyzed data | This paper | https://singlecell.broadinstitute.org/single_cell/study/SCP3331 |
| BCR sequences | This paper | https://doi.org/10.5281/zenodo.17603995 |
| **Cell lines** | | |
| HEK 293F | Thermo Fisher | Cat# R790-07; RRID: CVCL_6642 |
| **Experimental models: Organisms/strains** | | |
| Mouse: CD4bs-Int$^{1}$ BCR mouse model | This paper | N/A |
| Mouse: CD4bs-Int$^{2}$ BCR mouse model | This paper | N/A |
| Mouse: CD4bs-Int$^{3}$ BCR mouse model | This paper | N/A |
| Mouse: V2-Int$^{1}$ BCR mouse model | This paper | N/A |
| Mouse: V3-Int$^{1}$ BCR mouse model | This paper | N/A |
| Mouse: V3-Int$^{2}$ BCR mouse model | This paper | N/A |
| Mouse: B6.SJL-Ptprcapepcb/BoyJ | The Jackson Laboratory | JAX: 002014 |
| Mouse: C57BL/6J | The Jackson Laboratory | JAX: 000664 |
| **Recombinant DNA** | | |
| pHL-sec | N/A | Addgene #99845 |
| pCW-sec | N/A | N/A |
| pCW-CHIg-hG1 | N/A | N/A |
| pCW-CLIg-hk | N/A | N/A |
| **Software and algorithms** | | |
| BioRender | BioRender.com | https://biorender.com/ |
| Byos™ (Version 5) | Protein Metrics Inc. | https://www.proteinmetrics.com/products/byonic/ |
| Carterra Software | Carterra Inc. | N/A |
| Flowjo X | Treestar | https://www.flowjo.com/ |
| Geneious Prime | Biomatters | https://www.geneious.com/ |
| Fiji (ImageJ) | Schindelin et al.[104] | https://fiji.sc/ |
| Illustrator | Adobe | N/A |
| IMGT/V-quest | IMGT®, the international ImMunoGeneTics information system® (Université de Montpellier, CNRS, France) | http://www.imgt.org/IMGTindex/V-QUEST.php/ |
| Microsoft Office | Microsoft | https://www.office.com/ |
| Orbitrap Fusion Tune application v3.1 | Thermo Fisher Scientific | N/A |
| Prism 8 | GraphPad | https://www.graphpad.com/ |
| Python version 3.9.19 | The Python Software Foundation (PSF) | https://www.python.org/; RRID: SCR_008394 |
| R version 4.5.0 | R Foundation for Statistical Computing | https://www.r-project.org; RRID: SCR_001905 |
| Robust decomposition of cell type mixtures | Cable et al., 2022a[63] | https://doi.org/10.1038/s41587-021-00830-w |

(*Continued on next page*)

*Continued*

| REAGENT or RESOURCE | SOURCE | IDENTIFIER |
|---|---|---|
| Rstudio version 2025.05.0+496 | Rstudio, Inc. (2019) | https://posit.co; RRID: SCR_000432 |
| Scanpy | Wolf et al.[105] | https://github.com/theislab/scanpy; RRID: SCR_018139 |
| TissueFAXS SL 7.1.135 Confocal | TissueGnostics | |
| TissueFAXS SL Viewer 7.1.6245.135 | TissueGnostics | |
| UCSF ChimeraX v1.10.1 | Goddard et al.[106] | N/A |
| XCalibur Version v4.2 | Thermo Fisher Scientific | N/A |
| Custom analysis scripts | This paper | https://github.com/immunoliugy/affinity_brake |
| **Other** | | |
| Amicon® Ultra Centrifugal Filter, 100 kDa MWCO (15 mL) | Millipore Sigma | Cat# UFC9100 |
| Amicon® Ultra Centrifugal Filter, 100 kDa MWCO (4 mL) | Millipore Sigma | Cat# UFC8100 |
| Amicon® Ultra Centrifugal Filter, 30 kDa MWCO (15 mL) | Millipore Sigma | Cat# UFC9030 |
| Amicon® Ultra Centrifugal Filter, 30 kDa MWCO (4 mL) | Millipore Sigma | Cat# UFC8030 |
| Dawn HELEOS II | Wyatt | N/A |
| EasySpray PepMap RSLC C18 column (75 µm x 75 cm) | Thermo Fisher Scientific | Cat# ES805 |
| Endosafe nexgen-PTS Instrument | Charles River | N/A |
| HisTrap HP column (5 mL) | Cytiva | Cat# 17524801 |
| Microdialysis plate 48-wells 1 mL | Thermo Fisher Scientific | Cat# A50466 |
| NanoDrop 2000c Spectrophotometer | Thermo Fisher Scientific | ND-2000 |
| Oasis MCX 96-well µElution Plate | Waters | 186001830BA |
| Octet RED96e Instrument | FortéBio | RED96E |
| Optilab T-REX | Wyatt | N/A |
| Orbitrap Eclipse mass spectrometer | Thermo Fisher Scientific | N/A |
| Superdex 200 10/300 GL | Cytiva/GE | Cat# 17517501 |
| Ultimate 3000 HPLC | Thermo Fisher Scientific | N/A |
| Vivaspin 500, 3 kDa MWCO, Polyethersulfone | Sigma-Aldrich | Cat# GE28-9322-18 |

## EXPERIMENTAL MODEL AND SUBJECT DETAILS

$H^{N6\text{-}I3/N6\text{-}I3}\kappa^{N6\text{-}I3/N6\text{-}I3}$ (CD4bs-Int$^1$), $H^{min12A21/min12A21}\kappa^{min12A21/min12A21}$ (CD4bs-Int$^2$), $H^{N6\text{-}I2/N6\text{-}I2}\kappa^{N6\text{-}I2/\ N6\text{-}I2}$ (CD4bs-Int$^3$), $HPCT64^{\text{-}18D/PCT64\text{-}18D}\kappa^{PCT64\text{-}18D/PCT64\text{-}18D}$ (V2-Int$^1$), $H^{minBG18.6/minBG18.6}\kappa^{WT/WT}$ (V3-Int$^1$), and $H^{minBG18.11/\ minBG18.11}\kappa^{WT/WT}$ (V3-Int$^2$) BCR transgenic mouse lines were generated on the background of C57BL/6J (CD45.2$^{+/+}$) mice, as described previously.[55,56] Note, the HC sequences for V3-Int$^1$ and V3-Int$^2$ differ from the previously published minBG18.6 and minBG18.11 HC sequences by one amino acid in the $J_H$ gene (ARNAIRIYGVVALGEWFHYGMDVWGQGTAVTVSS for V3-Int$^{1/2}$; ARNAIRIYGVVALGEWFHYGMDVWGQGTTVTVSS for minBG18.6/11).[40] All transgenic mouse lines were generated in the animal facility of the Gene Modification Facility (Harvard University). Subsequent breeding, colony maintenance, and experimental procedures were performed at the animal facility of the Ragon Institute of Mass General Brigham, MIT, and Harvard. For experiments, wild-type (WT) adult male B6.SJL-Ptprca Pepcb/BoyJ (CD45.1$^{+/+}$) mice between the age of 8–12 weeks were purchased from The Jackson Laboratory (Bar Harbor, ME). Experimental mice were housed at the animal facility of the Ragon Institute with free access to food and water, controlled temperature, and a 12:12 hour light-dark cycle. All animal experiments were conducted in accordance with the Institutional Animal Care and Use Committee (IACUC) of Massachusetts General Hospital (MGH)'s approved Animal Study Protocols 2016N000286 and 2016N000022. The MGH Center for Comparative Medicine (CCM) is an Association for Assessment and Accreditation of Laboratory Animal Care (AAALAC) International-approved program.

## METHOD DETAILS

### Immunogen and probe design

In this work we sought to employ native-like immunogens derived from wild-type HIV-1 isolates to present unmodified epitopes capable of engaging moderately evolved broadly neutralizing antibodies (bnAbs) targeting diverse neutralizing supersites on Env: CD4-binding site (CD4bs), V2-apex (V2), and V3-glycan (V3). We selected Env from two strains whose soluble antigens fulfill two independent criteria to evaluate how affinity differences on both the antigen and BCR sides influence antibody feedback mechanisms: (1) Env-1 must show detectable binding affinity to the diverse minimally mutated bnAbs of interest (PCT64-18, minBG18.6, minBG18.11, min12A21 and N6-I3), and (2) Env-2 must display significantly lower affinity than Env-1 for CD4bs antibodies. BG505 (clade A) and DU172-17 (clade C) served as Env-1 and Env-2, respectively, fulfill these criteria (Figures S6B and S6C). BG505 MD39.3 construct design and characterization was previously described.[58] DU127-17 was selected because it is resistant to neutralization by several CD4bs-targeting bnAbs and its recombinant antigens display low affinity against VRC01-class bnAbs.[52,107] DU172 MD39.2 was designed using established HIV-1 Env stabilization strategies: (1) SOSIP mutations for improved stability,[108–110] (2) C-terminal truncation at residue D664 for enhanced homogeneity of trimeric pre-fusion gp140,[110,111] (3) MD39 mutations for improved antigenic profile, expression yield, and thermostability,[39] and (4) replacement of the furin cleavage site with a non-cleavable linker termed link14 between gp120 and gp41 (linker sequence: SHSGSGGSGSGGHA),[40] where we use the terminology MD39.2 to denote a cleavage-independent MD39 stabilized trimer (Figure S6A).[58] Mass spectrometry analysis and antigenic profiling against a panel of neutralizing and non-neutralizing antibodies performed by BLI confirmed DU172 MD39.2 constructs exhibit the expected N-linked glycan profile and adopt a trimeric pre-fusion conformation (Figures S6B–S6D).

Probes for BG505 and DU172 were generated by addition of His-Avi-tag (HHHHHHGGSGGSGLNDIFEAQKIEWHE) and His-tag (HHHHHH) sequences at the C terminus of gp41 after residue D664. while His-tagged trimers served as ELISA probes, and His-Avi-tag SOSIP served as FACS probes.

His- and His-Avi-tagged epitope-specific KO reagents were generated by introducing four VRC01-class-specific KO mutations (280R, 365L, 368R, and 371R) onto BG505 MD39.3 and DU172 MD39.2 SOSIP trimers as previously described.[90,112] His-Avi-tagged V2-apex epitope-specific KO mutants were created by introducing R169E and K171E mutations that abrogate binding by long-HCDR3 Apex bnAbs and related precursors.[96] His-Avi-tagged V3-glycan epitope-specific KO variants were produced by introducing R327D, H330K and N332T mutations.[40] All HIV-1 Env residues are denoted using HxB2 numbering.

### Immunogen, probe, and Ab production

For protein immunogen production, untagged trimeric immunogens were produced by transient transfection of HEK-293F cells (ThermoFisher) and purified by gravity-flow affinity chromatography using *Galanthus nivalis* lectin resin (Vectorlabs) followed by SEC using Superdex 200 Increase 10/300 GL columns (Cytiva). The homogeneity and molecular weight of antigens was confirmed by size-exclusion chromatography-multi-angle light scattering (SEC-MALS) in PBS using Superdex 200 Increase 10/300 GL columns (Cytiva) with an isocratic flow of 0.5 mL/min followed by DAWN HELEOS II and Optilab T-rEX detectors (Wyatt Technology). Endotoxin levels in immunogen preparations were confirmed to be <5 EU/mg of endotoxin using an Endosafe nexgen-PTS instrument (Charles River).

For mRNA immunogen production, the amino acid sequence encoding BG505 MD39.3 (gp151) was provided to Moderna for production and formulation of mRNA-LNP immunogens.

For probe production, His-tagged and His-Avi-tagged trimeric antigens were produced by transient transfection of HEK 293F cells (ThermoFisher) and purified by immobilized metal ion affinity chromatography (IMAC) using HisTrap excel columns 5 mL (Cytiva) followed by size-exclusion chromatography (SEC) using Superdex 200 Increase 10/300 GL columns (Cytiva). The homogeneity and molecular weight of antigens was confirmed by size-exclusion chromatography-multi-angle light scattering (SEC-MALS) in PBS using Superdex 200 Increase 10/300 GL columns (Cytiva) with an isocratic flow of 0.5 mL/min followed by DAWN HELEOS II and Optilab T-rEX detectors (Wyatt Technology). Biotinylation of His-Avi-tagged trimers was performed using BirA (Avidity) and purified by SEC with Superdex 200 Increase 10/300 GL columns (Cytiva) to remove unconjugated biotin molecules.

For Ab production, sequences encoding the antibody Fv regions were synthesized by GenScript and cloned into antibody expression vectors pCW-CHIg-hG1 and pCW-CLIg-hk for heavy and light chain genes, respectively. Monoclonal antibodies (mAbs) were produced using transient transfection of HEK 293F cells (ThermoFisher) and purified by gravity-flow affinity chromatography using rProteinA Sepharose Fast Flow resin (Cytiva). Min12A21, N6-I3, minBG18.6, and minBG18.11 antibody mutants were produced by GenScript using the TurboCHO expression service. All antibodies were produced as human IgG1s.

SMNP was provided by the Irvine lab of Scripps Research Institute.[59]

### Bio-layer interferometry (BLI)

Native-like conformation of soluble DU172 gp140 antigens was confirmed by Bio-Layer Interferometry (BLI) using a panel of broadly neutralizing (quaternary-specific PGT151 and PGT145; V3-specific PGT121; CD4bs-specific N6 and min12A21) and non-neutralizing antibodies (CD4bs-specific F105 and B6; V3-specific 19b) and conducted on an Octet RED Instrument (FortéBio). Non-neutralizing antibodies bind non-native trimers and monomeric gp120; BG505 gp120 foldon trimer served as a negative control representing poorly assembled Envs (binding to non-nAbs and lack of binding to quaternary-specific bnAbs). Monoclonal antibodies were captured on anti-hIgG Fc capture (AHC) biosensors (Sartorius) at a concentration of 10 μg/mL in kinetics buffer (PBS, pH 7.4,

0.01% [w/v] BSA, and 0.002% [v/v] Tween 20) for 120 seconds after baseline determination. Association was measured for 120 seconds by dipping IgG-loaded biosensors into wells containing 1 μM recombinant SOSIP trimers. Dissociation was monitored for 120 seconds in kinetics buffer. Relative binding was determined by subtracting baseline absorbance and calculating the maximum response (nm) at endpoint of the association phase.

Biotinylated sort reagents of BG505 MD39.3, BG505 MD39.3 CD4bs-KO, DU172 MD39.2, and DU172 MD39.2 CD4bs-KO were loaded onto streptavidin (SA) biosensors (Sartorius) at 25 μg/mL in kinetics buffer for 120 seconds after baseline determination. After reacquiring a kinetics buffer baseline, biosensors were transferred to wells containing 1 μM monoclonal antibodies (neutralizing and non-neutralizing IgGs) and allowed to associate for 120 seconds. The biosensors were dipped into kinetics buffer alone to monitor dissociation for additional 120 seconds. Relative binding was determined by subtracting baseline absorbance values from end-point measurements.

### Site-specific glycan profiling

N-linked site-specific glycan profiling was conducted as previously described to determine the degree of glycan occupancy and the extent of glycan heterogeneity (proportion of complex vs oligomannose/hybrid glycan types).[113]

### Surface Plasma Resonance (SPR)

We measured kinetics and affinity of antibody-antigen interactions on Carterra LSA using CMDP Sensor Chip (Carterra) and 1x HBS-EP$^+$ pH 7.4 running buffer (20x stock from Teknova, cat. no H8022) supplemented with BSA at 1 mg/mL. The chip surface for ligand capture was prepared following Carterra software instructions. About 800–1000 RU of capture antibody (SouthernBiotech cat.no 2047-01) in 10 mM sodium acetate pH 4.5 was amine coupled, and regeneration buffer Phosphoric Acid 1.7% was injected three times per cycle for 60 seconds. Ligand concentrations of 1 μg/mL were used with a contact time of 5 minutes. Analyte samples (SOSIP trimers) were buffer exchanged into the running buffer using dialysis and analyte concentrations were quantified on NanoDrop 2000c Spectrophotometer (Thermo Fisher Scientific) using absorption signal at 280 nm. Raw sensograms were analyzed using Kinetics software (Carterra), interspot and blank double referencing, Langmuir model. We typically cover a broad range of affinities in our runs and the best referencing practices differ depending on how fast the dissociation rate is for a particular ligand. For fast dissociation rates (faster than $9e^{-3}$ 1/s) we use automated batch referencing that includes overlay y-align and higher analyte concentrations. For slow dissociation rates ($9e^{-3}$ 1/s or less) we use manual process referencing that includes serial y-align and lower analyte concentrations. After automated data analysis by Kinetics software, we also performed additional filtering to remove datasets with highest response signals smaller than signals from negative controls. This additional filtering was performed automatically using an R-script (available upon request).

### B cell in vitro stimulation assay

Naive live B cells were purified from spleens of BCR transgenic and WT mice to reach more than 90% purity using negative B-cell isolation (Miltenyi Biotec). $10^7$ per mL B cells were labeled with 2 μM CFSE (Thermo Fisher) for 5 min at 37°C then were washed with complete B cell medium [RPMI supplemented with 10% FCS, 25 mM Hepes, GlutaMAX, Non-Essential Amino Acids, penicillin streptomycin (Thermo Fisher), and 50 μM β-mercaptoethanol (MilliporeSigma)]. CFSE Labelled cells were then stimulated in complete B cell medium supplemented with combinations of 10 ng/mL IL4 (R and D Systems), 10 ng/mL IL5 (R and D Systems), and 50 ng/mL CD40L (R and D Systems). After 3 days of culture, proliferation status was measure by percentages of CFSE$^{low}$ cells in flow cytometry based on CFSE levels at day 0 for each well. Survival status was measure by percentages of DAPI$^-$ cells after staining with DAPI (Thermo Fisher Scientific). The differentiation of plasmablasts was measured by percentages of CD138$^+$ cells after CD138 (281–2) staining.

### Adoptive transfer and immunization

For adoptive transfer, spleens were collected from donor BCR transgenic mice with a C57BL/6J (CD45.2$^{+/+}$) background. Spleens were crushed through a 70 μm cell strainer and subjected to pan B cell isolation kits (Miltenyi Biotec). Isolated B cells were then qualified for live cells on a LUNA-FX7 automated cell counter (Logos Biosystems) and adjusted to the desired number and volume (100 μl/mouse) in phosphate-buffered saline (PBS) before transfer to CD45.1$^{+/+}$ recipient mice by intravenous (i.v.) injection through the orbital sinus, establishing frequencies of 20 in $10^6$ B cells except where otherwise specified. For mRNA immunization, mRNA-LNP immunogens were diluted to desired quantity and volume in PBS. Unless otherwise stated, diluted mRNA was injected at 2 μg in 100 μl per mouse, intramuscularly (i.m.) through gastrocnemius, 50 μl each leg. For protein immunization, 10 μg immunogens mixed with 5 μg of SMNP adjuvant were immunized to each mouse in 100 μl PBS subcutaneously (s.c.), 50 μl at each side of tail base.

### Flow cytometry and cell sorting

For single cell suspensions, inguinal, popliteal, and iliac lymph nodes were crushed through a 70 μm cell strainer, centrifuged and resuspended in FACS buffer (2% fetal bovine serum/PBS). Single-cell suspensions were kept on ice after. Probes were conjugated with streptavidin-Alexa Fluor 488, streptavidin-Alexa Fluor 647, or streptavidin-Alexa Fluor 594 for at least 30 min. Cells were blocked by Fc block (clone 2.4G2, BD Biosciences) for 15 min and then pre-incubated with freshly conjugated specific probes for 15 min. Probe-stained cells were then co-incubated with surface antibodies for another 15 min. If sorting for 10x sequencing, cell barcodes (BioLegend) and anti-mouse CD45 hashtags (BioLegend) were incubated with cells for 15 min during the coincubation step. Cells

were washed 3 times with FACS buffer and re-suspended with DAPI 1:5000 diluted in FACS buffer, after which they were loaded into a BD LSR Fortessa analyzer or a BD FACS Aria Fusion sorter. Sorted cells were kept on ice for subsequent 10x sequencing procedures or at -80° for Sanger sequencing procedures. Data analysis was performed using FlowJo software (TreeStar).

### Single-cell BCR sequencing

For 10x Genomics single-cell BCR sequencing, bulk sorted cells were loaded onto the 10x Genomics Chromium Controller at 5,000–20,000 cells per reaction and encapsulated in gel beads in emulsion. Single-cell gene expression, V(D)J, and hash-tag oligo libraries were constructed using the Next GEM Single-cell 5′ Reagent Kits v2 (10x Genomics, Pleasanton, CA) following the manufacturer's protocol. Libraries were then quantified by Tapestation 4200 (Agilent, Santa Clara, CA) and the Qubit double-stranded DNA High Sensitivity assay (AAT Bioquest, Sunnyvale, CA). Qualified libraries were pooled and sequenced on the Nextseq2000 sequencer (Illumina, San Diego, CA). Finally, sequence data were analyzed using Cell Ranger pipelines and by customized analysis for specific BCR sequences.

For experiments with fewer cell numbers, single cell 96-well plate PCR was performed, as described previously.[12]

### LN homogenization and Enzyme-linked immunosorbent assays (ELISA)

To test IgG or IgM specific end point titers in LN, a homogenizing preparation step is needed prior to ELISA: one popliteal LN from each of the four mice in each group was carefully isolated and washed in PBS three times before all four were pooled into 100 μl of PBS with 1x Complete EDTA-free protease inhibitor cocktail (Roche). Pooled dLNs were homogenized on ice and centrifuged at 300 g, 4°C for 5 min. Supernatants were centrifuged again at 14000 g, 4°C for 10 min. Supernatants were transferred to a clean tube as prepared dLN homogenate and stored at -80°C for the next step.

Homogenate of dLN or mouse serum was then used for ELISA. Anti-His Ab (1 mg/ml, 50 μl per well) were incubated in 96-well high-absorption ELISA plates (NUNC/Corning) pre-coated with BG505 or epitope-specific-KO probes with His-tag (1 mg/ml, 50 μl per well) for 2 h at room temperature (RT). Plates were then washed 5 times with 0.05% Tween 20 in PBS (tPBS) and blocked with tPBS with 3% BSA for 2 h at RT. After washing, serial-diluted (2–5 folds depending on preliminary estimates of initial Ab titer) dLN homogenate or serum were incubated at 4°C for 4 h with requisite starting dilutions. Plates were washed again and incubated with 50 μl per well of alkaline phosphatase AffiniPure Goat anti-mouse IgG or IgM (Jackson ImmunoResearch) at 1:5000 in tPBS + 0.5 BSA FOR 1 h at RT. 50 μl per well of p-Nitrophenyl phosphate dissolved in ddH2O was added to each well for incubation of 20 min at RT for the final chromogenic reaction. Absorbance at 405 nm was determined with a Synergy Neo2 plate reader (BioTek). Endpoint titer was determined as dilution of the last serial-diluted well with an OD405 read over the threshold value, which was set as (mean + 3 x SD) of the OD405 read in all negative wells. A 5x dilution multiplier was applied to obtain the final est endpoint titer of dLNs.

### Immunofluorescence and histology

Frozen murine lymph node tissue sections were immersed in Harris hematoxylin for 15 seconds before rinsing in deionized (DI) water and washing in 1X PBS for 30 seconds. Sections were dipped in Scott's Tap water Substitute for 45 seconds and rinsed in DI water before they were dipped in 70% EtOH and 90% EtOH for 30 seconds each. Sections were immersed in alcoholic-eosin for 2 minutes and rinsed in DI water. Sections were dipped in 90% EtOH and 100% EtOH for 15 seconds each and dipped in 100% EtOH for 30 seconds. Sections were immersed in xylene for one minute, mounted, and coverslipped.

To verify the presence of adoptively transferred plasma cells in murine lymph node tissue sections, mounted 10 μm frozen tissue sections were fixed in 10% formalin for 10 minutes and washed three times in 1X PBS. Sections were permeabilized in 0.1% Triton X-100 for 15 minutes and washed three times in 1X PBS. Sections were stained with antibodies for adoptively transferred cells (Alexa Fluor 488 anti-mouse CD45.2, 104, BioLegend, 1:200), B cells (Alexa Fluor 594 anti-mouse/human CD45R/B220, RA3-6B2, BioLegend, 1:200), and plasma cells (Alexa Fluor 647 anti-IRF4, 3E4, BioLegend, 1:200) for one hour at room temperature. Sections were washed three times in 1X PBS, mounted, and coverslipped. Confocal imaging was performed on the TissueFAXS SL Q (TissueGnostics).

### Spatial transcriptomics: sample processing

Fresh frozen murine lymph node tissues were embedded in Tissue-Tek OCT compound and frozen on dry ice before transferring to -80°C for long-term storage. Frozen blocks were warmed to -20°C in a cryostat (Leica CM3050S) for 30 min prior to handling. Tissues were sliced at a 10 μm thickness and Slide-seq was performed on the fresh frozen sections as previously described.[114] Serial sections were taken for tissue staining at a later time. Spatial libraries were sequenced on an Illumina NextSeq 2000 P3 flow cell with the following read structure: 42 bases Read 1, 8 bases Index 1, 41 bases Read 2, 0 bases Index 2. Each library received approximately 250 million reads.

### Spatial transcriptomics: data analysis

As a quality control measure, we first removed beads with a unique molecular identifier (UMI) count of less than 100. Next, to delineate tissue boundaries and remove off-tissue beads, we performed Density Based Spatial Clustering of Applications with Noise (DBSCAN).[115] To ensure tissue regions were continuous, we subsequently performed dilation, whereby beads initially removed by DBSCAN were added back to the tissue if they were located within a small radius of on-tissue beads.

Robust Cell Type Decomposition (RCTD)[63] was used to assign cell types (plasma cell (PC), germinal center B cell (GCBC), cytotoxic T cell (cytotoxic), follicular dendritic cell (FDC), myeloid cell (myeloid), CD4 T cell (CD4), naive B cell (NBC), memory B cell (MBC), epithelial cell (Epithelial), T follicular regulatory cell (Tfr), T follicular helper cell (Tfh), and plasmacytoid dendritic cell (PDC)) as singlets or doublets to each bead on Slide-seq data from lymph node samples. Mouse orthologs of human genes were identified using Ensembl BioMart[116] based on reference scRNA-seq datasets.[64]

Germinal center regions were identified through marker gene expression (*Bcl6, Aicda, Rgs13*, and *Stnb1m*) and RCTD cell type assignments, including beads classified by RCTD as GCBC singlets or doublets containing GCBCs. These masks were merged, followed by DBSCAN clustering and spatial dilation. Plasma cells annotated as "PC in GC" or "PC outside GC" were retained following high-confidence filtering (singlets and confidently assigned doublets).

### Statistical analysis

For Slide-seq data, analyses were conducted in Python 3.9.19 (The Python Software Foundation). For each gene/feature, pairwise group comparisons were performed using two-sided Mann–Whitney U tests. *P*-values were then adjusted for multiple testing using the Holm–Bonferroni correction.

All other statistical analyses were performed using Prism 10 (GraphPad). Normal distribution was not assumed. For comparisons involving two groups, Mann-Whitney's test was utilized. For comparisons involving three or more groups, q-values were calculated by either 2-way analysis of variance (ANOVA) or nonparametric ANOVA (Kruskal-Wallis tests), as indicated in the legends; this was followed by post-hoc pairwise comparisons with Benjamini-Krieger-Yekutieli (BKY) correction for head-to-head comparisons.

Adjusted *p*-values (q-values) are indicated as follows: $^{*}p < 0.05$, $^{**}p < 0.01$, $^{***}p < 0.001$, $^{****}p < 0.0001$; ns = not significant.